Alexandria Engineering Journal (2023) 76, 101–130

HOSTED BY

Alexandria University

Alexandria Engineering Journal

www.elsevier.com/locate/aej
www.sciencedirect.com

ORIGINAL ARTICLE

Darcy-Forchheimer hybrid nanofluid flow over the rotating Riga disk in the presence of chemical reaction: Artificial neural network approach

Bhupendra K Sharma [a,*], **Parikshit Sharma** [a], **Nidhish K Mishra** [b], **Unai Fernandez-Gamiz** [c]

[a] *Department of Mathematics, Birla Institute of Technology and Science, Pilani Campus, Rajasthan 333031, India*
[b] *Department of Basic Sciences, College of Sciences and Theoretical Studies, Saudi Electronic University, Riyadh 11673, Saudi Arabia*
[c] *Department of Nuclear and Fluid Mechanics, University of the Basque Country (UPV/EHU), Nieves Cano 12, 01006 Vitoria-Gasteiz, Spain*

Received 25 March 2023; revised 2 June 2023; accepted 6 June 2023
Available online 17 June 2023

KEYWORDS

Hybrid nanoparticles;
Rotating disk;
Heated Riga surface;
Viscous dissipation;
Joule heating;
Artificial neural network

Abstract The aim of present study is to examine the augmentation of thermal energy transfer in hybrid nanofluid flow caused by a rotating Riga disk in the presence of thermal radiation and chemical reaction. The silver and aluminium oxide nanoparticles are used to examine the thermal effect of water base fluid. The Darcy-Forchheimer model is considered to endorse the inertial and porous media effects and makes the model more realistic from the physical scenario. Levenberg-Marquardt backpropagation algorithm is considered to analyze the hybrid nanofluid's properties. Using scaling group transformations, the governing partial differential equations are transformed into a system of ordinary differential equations. Resulting ordinary differential equations are solved numerically by applying a suitable shooting technique by MATLAB. The results obtained for the governing differential equations have been incorporated into a dataset on which the neural network has been trained. The effects of physical parameters have been analyzed for velocity, temperature, and concentration profiles. The determination, designing, convergence, verification, and stability of the Levenberg-Marquardt backpropagation neural network algorithm are validated on the assessment of achieved accuracy through performance, fit, regression, and error histogram plots for the discussed hybrid nanofluid. It is observed that fluid velocity reduces for enhanced Darcy-Forchheimer number, magnetic parameters and boosted for enhanced modified Hartmann number. Temperature profile increases by increasing the Brownian motion and thermophoresis parameters.

* Corresponding author.
E-mail addresses: bhupen_1402@yahoo.co.in, bksharma@pilani.bits-pilani.ac.in (B.K Sharma), parikshitsharma2001@gmail.com (P. Sharma), n.kumar@seu.edu.sa (N.K Mishra).

Peer review under responsibility of Faculty of Engineering, Alexandria University.

https://doi.org/10.1016/j.aej.2023.06.014
1110-0168

Nomenclature

Abbreviations

f	Fluid
nf	Nanofluid
hnf	Hybrid nanofluid
ODEs	Ordinary differential equations
PDEs	Partial differential different equations
LMBP	Levenberg–Marquardt backpropagation
NN-LMBP	Neural networks Levenberg-Marquardt back-propagation

Symbols

(U, V, W)	Velocity components (m/s)
(z, φ, r)	Cylindrical coordinates
v	Kinematic viscosity (m^2/s)
k_0	Permeability of porous medium ($m^{2)}$
F_0	Porous medium coefficient
C_b	Drag force coefficient
σ	Electrical conductivity (S/m)
ρ	Density (kg/m^3)
B_0	Magnetic field strength (T)
M_0	Riga plate (external) magnetic field strength (T)
j_0	Current density (A/m^2)
a_0	Riga plate constant
T	Temperature (K)
k	Thermal conductivity (W/m K)
c_p	Specific heat (J/(kg K))
s	Shape factor
σ^*	Stefan - Boltzmann constant
k^*	Absorption coefficient (1/m)
T_∞	Ambient temperature (K)
T_f	Disc temperature (K)
Q_0	Heat source (J)
μ	Dynamic viscosity (kg/(ms))
τ	Ratio of effective heat capacity of the nanoparticle material to that of base fluid
D_B	Brownian diffusion coefficient
C	Concentration (kg/m^3)
D_T	Thermophoretic diffusion coefficient
C_∞	Ambient concentration (kg/m^3)
k_r^2	Chemical reaction rate constant
ω	Constant angular velocity (R/s)
η	Similarity transformation coordinate
ϕ_1	Volume fraction of Al_2O_3
ϕ_2	Volume fraction of Ag
F′	Dimensionless radial velocity
G	Dimensionless azimuthal velocity
θ	Dimensionless temperature
ϕ	Dimensionless concentration

1. Introduction

Nanofluids are characterized as having a high concentration of ultrafine particles suspended in a liquid at lower concentrations. These fluids possess thermophysical properties that are superior to pure liquid carriers. Khan [1,2] explored the effects of nanoparticles on blood flow dynamics using Atangana, Baleanu, and Prabhakar fractional derivative mathematical models. Many researchers have studied fluid flow problems in various mediums. Khan [3] examined the hemodynamic of blood flow over an inclined cylinder. The findings contribute to our understanding of the behavior of blood flow over inclined surfaces. Izady et al. [4,5] investigated an aqueous hybrid nanofluid containing Fe_2O_3 and CuO nanoparticles over a permeable stretching/shrinking surface. Magnetic fields play a crucial role in nanofluids by providing an additional means of controlling and manipulating the behavior and properties of nanoparticles suspended in a fluid. Khan [6] investigates the impact of ramped temperature on the dynamics of unsteady viscoelastic fluids under the influence of the Lorentz force. The findings emphasize the significance of considering temperature variations when analyzing the behavior of viscoelastic fluids under magnetic fields. Dinarvand et al. [7] investigated the magnetohydrodynamic (MHD) flow of a hybrid nanofluid consisting of MgO-Ag particles in water past a moving slim needle, contributing to the accurate measurement of fluid properties. Khan et al. [8] presented an exact solution for the flow of a hybrid nanofluid considering the influence of Lorentz forces, under the combined effects of magnetic fields and particle suspensions. Mohanty et al. [9] studied the effects of an inclined magnetic field on the thermo-solutal Marangoni stagnation point flow of a hybrid nanofluid.

Heat transfer and mass transfer in nanofluids offer improved thermal conductivity and enhanced mass transfer properties, making them valuable in various fields. Khan [10] studied the influence of ramped heating on the thermal conductivity and stability of nanofluids. Ilyas Khan [11] provided insights into the heat transfer characteristics of nanofluids in inclined plane geometries, aiding in the optimization of heat transfer processes in various engineering applications. Dinarvand et al. [12] introduced a mass-based hybrid nanofluid model to analyze heat transfer in the flow over a convectively warmed moving wedge, providing insights into the thermodynamic behavior of nanofluids and their impact on heat transfer and fluid flow. Mebarek-Oudina et al. [13] provided a comprehensive review of the applications of nano-fluids and various heat transfer enhancement techniques in different enclosures to improve heat transfer performance. The shape of nanoparticles is important in nanofluids due to its influence on the overall properties and behavior of the fluid. Dinarvand et al. [14] examine the effects of shape factors on the flow behavior, providing valuable insights into the role of particle shape in the performance and characteristics of hybrid nanofluids. Samantaray et al. [15] investigated the Darcy-Forchheimer up/down-flow of entropy optimized radiative nanofluids, paying special attention to the shape effects. Ghadikolaei et al. [16,17,18] explored various shape factor effects on three types of nanofluids.

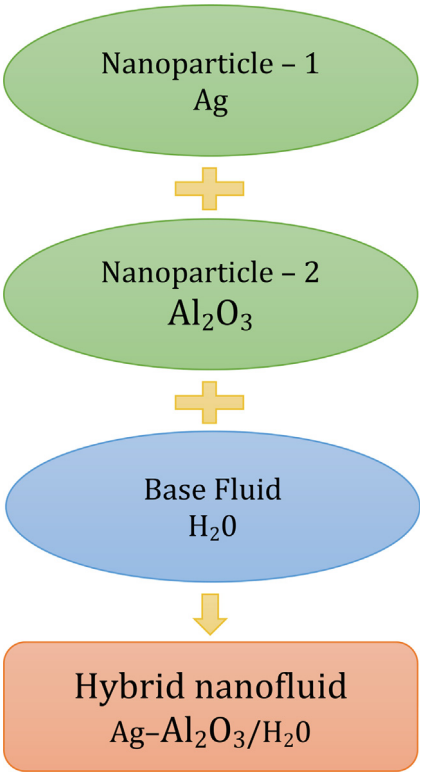

Fig. 1a Hybrid nanofluid preparation.

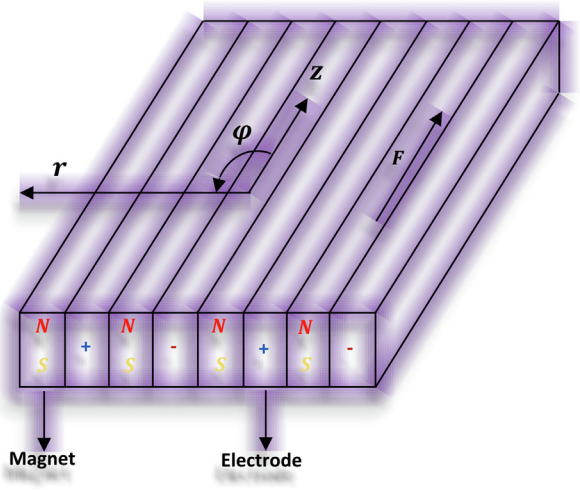

Fig. 1b Physical view of the Riga plate.

Porous medium plays an important role in nanofluids by providing a structure with interconnected void spaces for the dispersion and flow of nanoparticles. Dinarvand et al. [19] examined the flow characteristics of a hybrid nanofluid over a nonlinearly stretching permeable sheet in a porous medium. The study highlighted the heat transfer characteristics of hybrid nanofluid, contributing to the understanding of nanofluid dynamics in porous media applications. Ilyas et al. [20] explored the Cu-Al_2O_3/H_2O hybrid nanofluid in a porous medium over a rotating disc with joule heating and viscous dissolution. Raja et al. [21] investigated the flow characteristics of a magnetized convective Casson liquid through a porous channel. Ghadikolaei et al. [22,23,24,25] explored the porous nature with different shapes on four types of nanofluids. Riga plate surface is important in nanofluids as it provides a controlled and well-defined surface for studying the behavior and properties of nanoparticles dispersed in fluids. Shafiq et al. [26] performed a sensitivity analysis of nanofluids over a radiative Riga surface, providing insights into the influential parameters affecting the flow characteristics. The Riga surface has been explored by many other researchers for hybrid nanofluids [27,28,29,30,31]. Brownian motion is important in nanofluids as it leads to the dispersion and stability of nanoparticles by providing random motion, preventing particle aggregation. Thermophoresis, on the other hand, influences the distribution of nanoparticles in a temperature gradient, playing a role in the heat transfer characteristics of nanofluids. Dharmaiah et al. [32] explored the influence of Brownian motion and thermophoresis on the flow of Jeffrey fluids with nonlinear thermal radiation passing over a wedge in the context of nuclear reactor applications. Swaine et al. [33] studied the heat transport and stagnation-point flow of magnetized nanofluids, considering variable thermal conductivity, Brownian motion, and thermophoresis effects.

This Riga plate surface finds applications in enhanced heat transfer. The micro/nanostructures on the Riga plate surface disrupt the thermal boundary layer, improving heat transfer in nanofluids. It is beneficial for cooling systems, heat exchangers, and thermal energy storage. Anti-Fouling and Anti-Corrosion: The surface properties of the Riga plate prevent fouling and corrosion in nanofluid systems, improving system efficiency and reliability. The Riga plate's micro/nanostructures reduce drag and enable flow control, enhancing energy efficiency in transportation systems and microfluidic devices. Biomedical Applications: The Riga plate surface has biocompatibility and fluid manipulation capabilities, making it suitable for drug delivery systems, biomedical sensors, and tissue engineering applications. Thermal radiation plays a significant role in the overall heat transfer process by allowing energy to be exchanged between the nanoparticles and the surroundings. Chabani et al. [34] presented a numerical analysis of natural convective flow of a magnetic hybrid nanofluid in a trapezoidal enclosure with an adjusted porous medium. Mebarek-Oudina et al. [35] investigated the convective heat transfer characteristics of Titania nanofluids with different base fluids in a cylindrical annulus configuration, considering the presence of heat sources and thermal radiation. Sahu et al. [36] studied the flow behavior under Darcy-Forchheimer flow conditions induced by a thermal radiations system. Nayak et al. [37] did numerical computations for entropy generation in the Darcy-Forchheimer transport of hybrid nanofluids in presence of thermal radiation. Ghadikolaei et al. [38,39,40,41,42,43] studied the thermal radiations effect on various types of nanofluids with different combined effects. Chemical reactions in nanofluids are important as they can influence the stability, reactivity, and functionality of nanoparticles, which in turn can impact the overall properties and performance of nanofluids. Samantaray et al. [44] investigated the behavior of chemically reactive and radiative Darcy/non-Darcy stagnation point flow of ternary composite nanofluids providing insights into the heat and mass transfer characteristics in such systems. Sahu et al. [45] examined the hydrothermal stagnation point flow of a Carreau nanofluid over a moving thin needle in a Darcy-Forchheimer

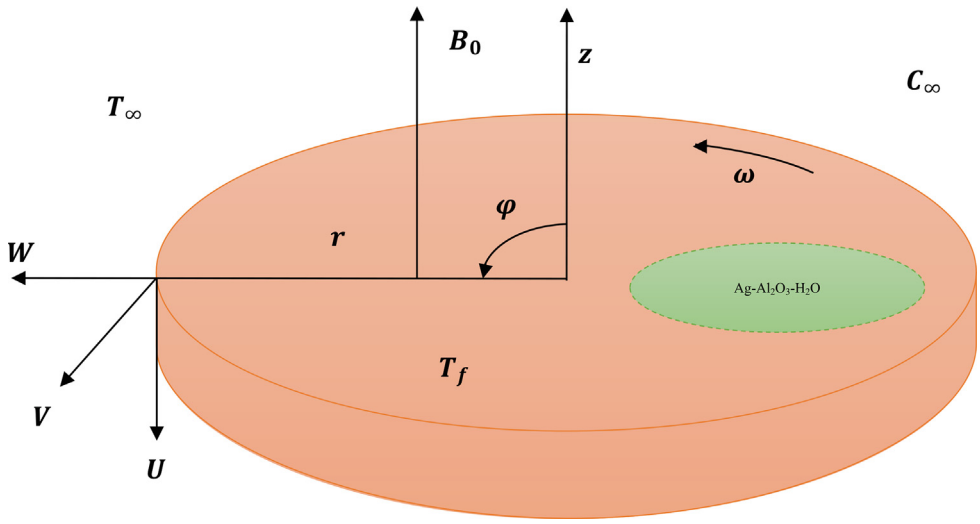

Fig. 1c Geometrical description of the problem.

Table 1 Thermophysical properties of hybrid nanofluid.

Properties	Notation	Nanoparticles		Base fluid
		Ag	Al_2O_3	H_2O
Specific heat (J/kg K)	C_p	235	765	4179
Density (Kg/m3)	ρ	10,500	3970	997
Thermal conductivity(W/m K)	k	429	40	0.613

medium, considering cubic autocatalytic chemical reactions. Joule heating is important in nanofluids as it contributes to the overall heat transfer process by converting electrical energy into thermal energy, thereby raising the temperature of the nanofluid, and influencing its thermal behavior. Mohanty et al. [46] did an analysis of irreversibility in the context of convective Darcy-Forchheimer Casson hybrid nanofluid flow induced by Joule heating. Sahu et al. [47] studied the thermal management of Darcy-Forchheimer single-walled carbon nanotube and multi-walled carbon nanotube cross hybrid nanofluid flow. Abbas et al. [48] presented a numerical investigation on heat transfer characteristics in hybrid nanofluid flow over a curved surface with Joule heating effects.

Due to high thermal conductivity, silver and aluminium oxide nanoparticles make good nanofluids. Silver nanoparticles don't agglomerate, keeping the nanofluid steady. Low-cost aluminium oxide is stable. Aluminium oxide nanoparticles are suitable for heat transfer and thermal management due to their dispersibility, specific surface area, and chemical stability. Also, combining silver and aluminium oxide gives a better hand by combining the unique properties of each nanoparticle. Additionally, using two nanoparticles can increase the flexibility of the nanofluid to be tailored for specific applications. The thermophysical properties of the nanoparticle are studied in a combined manner with the base fluid.

In today's world, neural networks (also called artificial neural networks) play a vital role in every domain of science and engineering for problem-solving. AAN is an adaptive system that learns using interconnected nodes or neurons in a layered structure that is similar in appearance to a human brain. Because neural networks can learn from their input data, they can be taught to recognize patterns, organize data, and predict the outcomes of future events. Nowadays ANNs are being used aggressively in the field of nanofluids. Shafiq et al. [49] explored the significance of machine learning algorithms in analyzing the flow of electromagnetic hydrodynamics graphene oxide, water, and ethylene glycol nanofluids in a Darcy-Forchheimer medium. Shafiq et al. [50] developed an artificial neural network (ANN) model to investigate nanofluid convective heat transfer through a moving needle. The investigation included the effects of Soret and Dufour's coefficients, and a highly accurate ANN model was trained to predict heat transfer performance. Shafiq et al. [51] created an ANN model to examine the effects of nanoparticle and solid–fluid interfacial layer on the flow of single-walled carbon nanotubes/ethylene glycol nanofluids through narrow slender needles. The study discovered that the ANN model accurately predicted the nanofluid's fluid flow characteristics and heat transfer performance. Shafiq et al. [52] used numerical and ANN modelling to examine the erratic hydromagnetic Williamson fluid flow on a radiative surface. The research found that the ANN model provided accurate predictions of the fluid flow and heat transfer performance, which can be applied to the design of heat transfer devices that are effective. Some good applications of ANNs can be found in the reliability of electrical components [53], reliability analysis using a mixture of

Lindley distributions [54], to study Soret and Dufour effects in chemical equations [55] COVID-19 data analysis [56].

On the basis of the literature survey performed above, no attempt has been made to accomplish thermal energy transfer in hybrid nanofluid flow caused by a rotating Riga disk in the presence of thermal radiation and chemical reaction. Based on literature review, it can be concluded that the following are the novelty of the present study:

- A novel mathematical model is developed utilizing hybrid nanofluid composed of nanoparticles Ag and Al_2O_3 with H_2O as the base fluid.
- Combined effects of porous medium, Riga surface, thermal radiation, joule heating, viscous dissipation, magnetic field, and chemical reaction is examined.
- Levenberg-Marquardt backpropagation algorithm is used to examine the hybrid nanofluid's performance, network training, regression, error histograms, and fit plots.

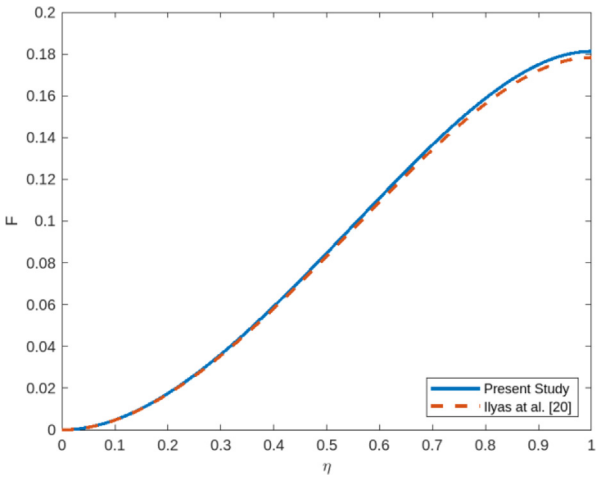

Fig. 2a Comparative analysis of.

2. Problem formulation

Considered an incompressible, steady, pseudoplastic, and electrically conducting Ag-Al_2O_3/H_2O hybrid nanofluid (as shown in Fig. 1a) passing through a rotating disc. Fluid flow is considered as highly porous medium subjected to a convectively heated Riga plate, thermal radiation, external magnetic field, and viscous dissipation. The mass transfer phenomena is considered by assuming a chemical reaction with k_r^2 as the rate of constant. The combination of electrodes and magnets to design the Riga plate for the present problem is illustrated in Fig. 1b. The cylindrical coordinate system (z, φ, r) is considered to formulate the physical model. The disc is placed in the $r-\varphi$ plane and the fluid flows in the increasing direction of z axis. It is assumed that the disc rotates about the positive φ direction with uniform angular velocity ω. The disc has a constant temperature T_w and the outside temperature is T_∞. The disc surface is stretching with a velocity of $U_w = r\omega$. A uniform magnetic field, $\overrightarrow{B_0} = (B_0, 0, 0)$, is applied parallel to the z-axis, where B_0 represents the strength of magnetic field. The physical model of the problem can be visualized in Fig. 1c. Due to the axial symmetry of the problem, the derivatives with respect to the coordinate φ are omitted. The governing equations of the fluid flow problem under above assumptions can be written as [57–60]:

$$\frac{\partial W}{\partial r} + \frac{\mathrm{W}}{r} + \frac{\partial U}{\partial z} = 0, \tag{1}$$

$$W\frac{\partial W}{\partial r} - \frac{V^2}{r} + U\frac{\partial W}{\partial z} = \nu_{hnf}\left(\frac{\partial^2 W}{\partial r^2} + \frac{1}{r}\frac{\partial W}{\partial r} - \frac{W}{r^2} + \frac{\partial^2 W}{\partial z^2}\right) - \nu_{hnf}\frac{W}{k_0} - F_0 W^2 - \frac{\sigma_{hnf}}{\rho_{hnf}}B_0^2 W + \frac{\pi}{8} \times \frac{j_0 M_0}{\rho_f} e^{\left(-\frac{\pi}{a_0}\right)z}, \tag{2}$$

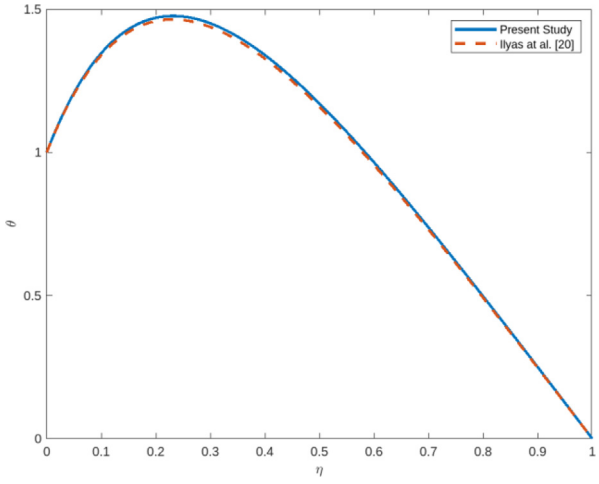

Fig. 2b Comparative analysis of..θ

$$W\frac{\partial V}{\partial r} + \frac{\mathrm{V.W.}}{r} + U\frac{\partial V}{\partial z} = \nu_{hnf}\left(\frac{\partial^2 V}{\partial r^2} + \frac{1}{r}\frac{\partial V}{\partial r} - \frac{V}{r^2} + \frac{\partial^2 V}{\partial z^2}\right) - \nu_{hnf}\frac{V}{k_0} - F_0 V^2 - \frac{\sigma_{hnf}}{\rho_{hnf}}B_0^2 V + \frac{\pi}{8} \times \frac{j_0 M_0}{\rho_f} e^{\left(-\frac{\pi}{a_0}\right)z}, \tag{3}$$

$$W\frac{\partial U}{\partial r} + U\frac{\partial U}{\partial z} = \nu_{hnf}\left(\frac{\partial^2 U}{\partial r^2} + \frac{1}{r}\frac{\partial U}{\partial r} + \frac{\partial^2 U}{\partial z^2}\right) - \nu_{hnf}\frac{U}{k_0} - F_0 U^2 \tag{4}$$

Table 2 Comparative study of F and..θ

η	0.000000	0.200000	0.400000	0.600000	0.800000	1.000000
F (Present study)	0.000000	0.016268	0.054116	0.102055	0.155561	0.177550
F (Ilyas et al. [20])	0.000000	0.016268	0.054116	0.102053	0.155560	0.177551
[03B8](Present study)	1.000000	0.909069	0.752077	0.549457	0.300000	0.000000
[03B8](Ilyas et al. [20])	1.000000	0.909069	0.752079	0.549458	0.300000	0.000000

Table 3 Various cases and values of dimensionless parameters.

Parameter	Case-1	Case-2	Case-3	Case-4
M	0.0	1.0	2.0	3.0
Fr	0.0	1.0	2.0	3.0
Rd	4.0	5.0	6.0	7.0
Ha	0.0	0.5	1.0	1.5
Nb	0.5	1.0	1.5	2.0
Nt	0.0	0.2	0.4	0.6
Kr	0.0	2.0	4.0	6.0
ϕ_1	0.0	0.01	0.02	0.03
ϕ_2	0.0	0.01	0.02	0.03

Table 4 Reference and default values of flow parameters.

Parameter	Range	Default	Reference
β	0–1	0.1	[20]
M	0–8	5	[69]
Fr	0–8	5	[68]
Rd	0–8	5	[67]
Br	0–6	4	[66]
Pr	0–20	6.9	[65]
ϕ_1	0–0.05	0.01	[20]
ϕ_2	0–0.05	0.01	[20]
Ha	0–6	2.5	[66]
γ	0–1	0.8	[69]
Nb	0.1–1	0.6	[65]
Nt	0–1	0.6	[65]
Sc	0–1	0.5	[70]
Kr	0–5	2.1	[68]
s	0–15	3.7	[70]

$$W\frac{\partial T}{\partial r}+U\frac{\partial T}{\partial z}=\left(\frac{\partial^2 T}{\partial r^2}+\frac{1}{r}\frac{\partial T}{\partial r}+\frac{\partial^2 T}{\partial z^2}\right)\left(\frac{\kappa_{hnf}}{\left(\rho C_{p_{hnf}}\right)}+5.333\frac{\sigma^* T_\infty^3}{k^*\left(\rho C_{p_{hnf}}\right)}\right)+\frac{\mathrm{B}_0^2\sigma_{\mathrm{hnf}}}{\left(\rho C_{p_{hnf}}\right)}(\mathrm{W}^2+\mathrm{V}^2)+\frac{\mu_{hnf}}{\left(\rho C_{p_{hnf}}\right)}\left[\left(\frac{\partial W}{\partial z}\right)^2+\left(\frac{\partial v}{\partial z}\right)^2\right]+\tau\left\{D_B\left[\frac{\partial T}{\partial r}\frac{\partial C}{\partial r}+\frac{\partial T}{\partial z}\frac{\partial C}{\partial z}\right]+\frac{D_T}{T_\infty}\left[\left(\frac{\partial T}{\partial r}\right)^2+\left(\frac{\partial T}{\partial z}\right)^2\right]\right\},\quad(5)$$

$$W\frac{\partial C}{\partial r}+U\frac{\partial C}{\partial z}=D_B\left(\frac{\partial^2 C}{\partial r^2}+\frac{1}{r}\frac{\partial C}{\partial r}+\frac{\partial^2 C}{\partial z^2}\right)+\frac{D_T}{T_\infty}\left(\frac{\partial^2 T}{\partial r^2}+\frac{1}{r}\frac{\partial T}{\partial r}+\frac{\partial^2 T}{\partial z^2}\right)-k_r^2(C-C_\infty)\quad(6)$$

The corresponding boundary conditions are [57]:

$$\left.\begin{aligned}W=0, V=r\omega, U=0, C=2C_\infty, T=T_w, atz=0\\ W\to 0, V\to 0, T\to T_\infty, C\to C_\infty asz\to\infty\end{aligned}\right\}\quad(7)$$

Where, $F_0=\frac{C_b}{rk_0^{0.5}}$ represents the porous medium coefficient. v_{hnf}, σ_{hnf}, and μ_{hnf} are kinematic viscosity, electrical conductivity, and dynamic viscosity of the hybrid nanofluid, respectively. For the considered hybrid nanofluid, the thermophysical properties are mentioned in Table 1 [4,5,14] and mathematically expressed as [63]:

$$\left.\begin{aligned}\frac{k_{hnf}}{k_{nf}}&=\frac{k_2+\phi_2(1-s)\left(k_{nf}-k_2\right)-k_{nf}(1-s)}{k_2+\phi_2\left(k_{nf}-k_2\right)+k_{nf}(1-s)},\\ \frac{k_{nf}}{k_f}&=\frac{k_1+\phi_1(1-s)\left(k_f-k_1\right)-k_f(1-s)}{k_1+\phi_1\left(k_f-k_1\right)+k_f(1-s)},\\ \frac{\sigma_{hnf}}{\sigma_{nf}}&=\frac{\sigma_2+\phi_2(1-s)\left(\sigma_{nf}-\sigma_2\right)-\sigma_{nf}(1-s)}{\sigma_2+\phi_2\left(\sigma_{nf}-\sigma_2\right)+\sigma_{nf}(1-s)},\\ \frac{\sigma_{nf}}{\sigma_f}&=\frac{\sigma_1+\phi_1(1-s)\left(\sigma_f-\sigma_1\right)-\sigma_f(1-s)}{\sigma_1+\phi_1\left(\sigma_f-\sigma_1\right)+\sigma_f(1-s)},\\ \frac{\mu_{hnf}}{\mu_f}&=\left[(1-\phi_1)(1-\phi_2)\right]^{-2.5},\\ \rho_{hnf}&=\left[(1-\phi_1)\rho_f+\phi_1\rho_1\right](1-\phi_2)+\phi_2\rho_2,\\ \left(\rho c_p\right)_{hnf}&=\left[(1-\phi_1)\left(\rho c_p\right)_f+\phi_1\left(\rho c_p\right)_1\right](1-\phi_2)+\phi_2\left(\rho c_p\right)_2\end{aligned}\right\}\quad(8)$$

The radiation term included in Eq. (4) can be obtained by using Rosseland estimation, q_r is mathematically expressed in the following way [61,62]:

$$q_r=-\frac{4}{3}\frac{\sigma^*}{k^*}\nabla T^{*4}$$

By assuming that the temperature diffusion inside the flow is sufficiently modest, the term T^{*4} can be expressed as a linear temperature function in the Taylor series with respect to T_0 and ignoring the higher expressions, we get:

$$T^{*4}\approx -3T_0^4+4T^*T_0^3$$

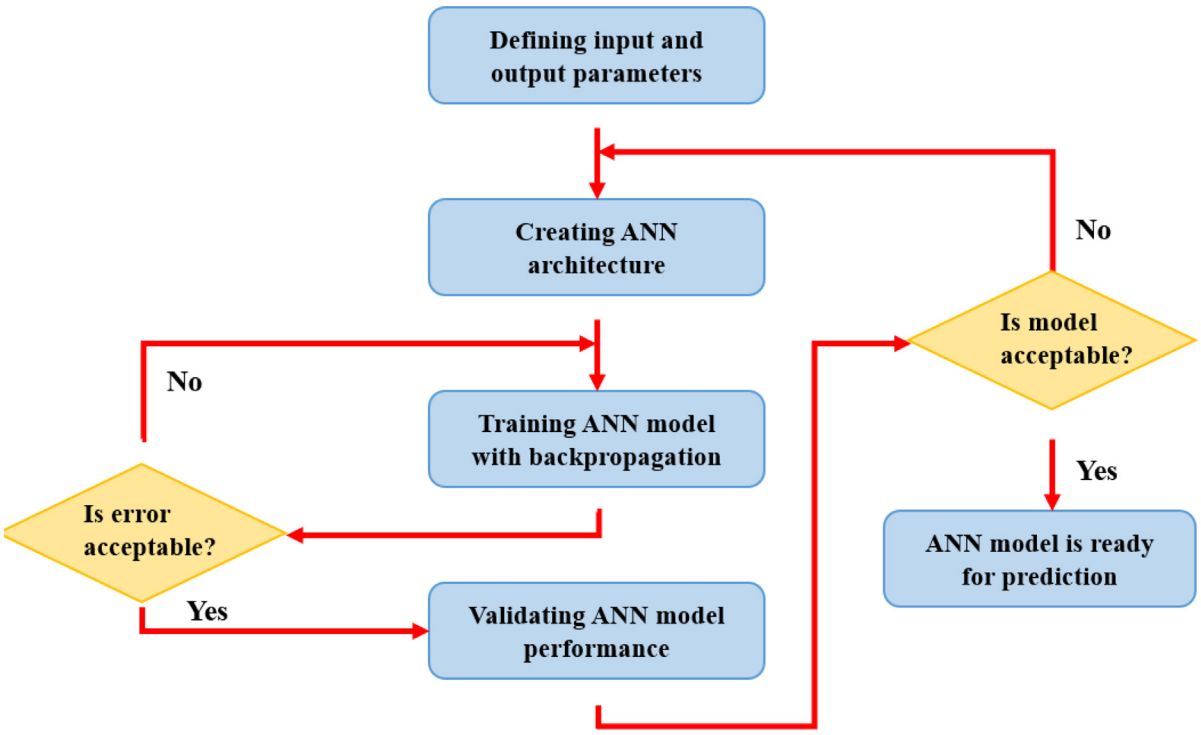

Fig. 2c Flow chart for ANN methodology.

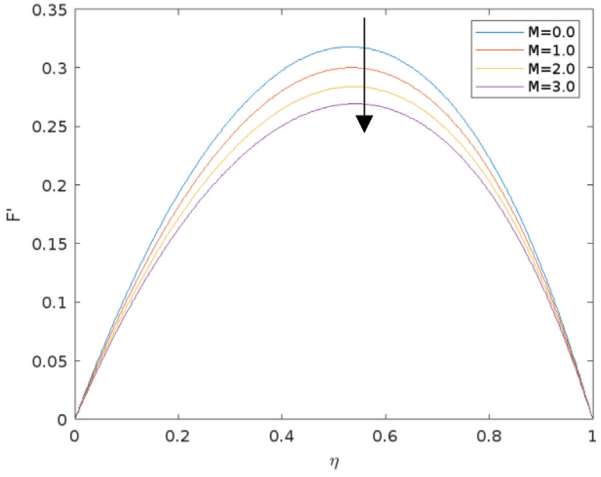

Fig. 3a Radial velocity VS Magnetic parameter.

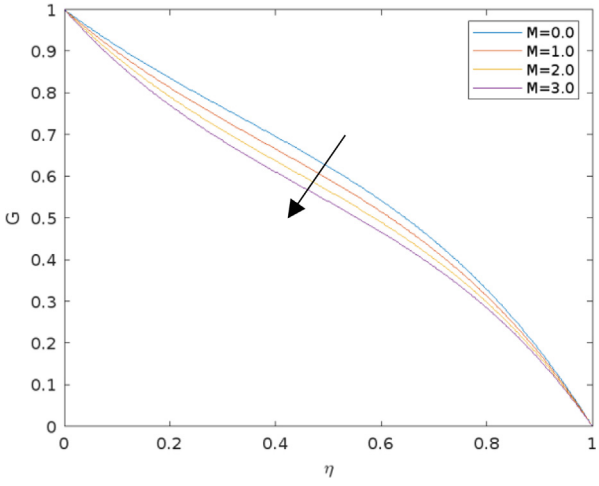

Fig. 3b Azimuthal velocity VS Magnetic parameter.

W, V, and U are the r, φ, and z velocity components, respectively. The following transformations are used to convert the system of partial differential equations (1) to (6) into ordinary differential equations:

$$W = r\omega F'(\eta),\quad V = r\omega G(\eta),\quad U = -\sqrt{\omega \nu_f}F(\eta),$$
$$\eta = \sqrt{\frac{\omega}{\nu_f}}z,\quad \theta(\eta) = \frac{\mathrm{T}-\mathrm{T}_\infty}{T_f - T_\infty},\quad \phi(\eta) = \frac{\mathrm{C}-\mathrm{C}_\infty}{C_\infty} \tag{9}$$

Equations (2–6) reduce into the following ordinary differential equations:

$$F''' - \beta F' = B_1 B_2\left(F'^2 - FF'' - G^2 + MF'^2 + FrF'^2 - Hae^{\gamma\eta}\right), \tag{10}$$

$$G'' - \beta G = B_1 B_2\left(2F'G - FG' + MG + FrG^2 - Hae^{\gamma\eta}\right), \tag{11}$$

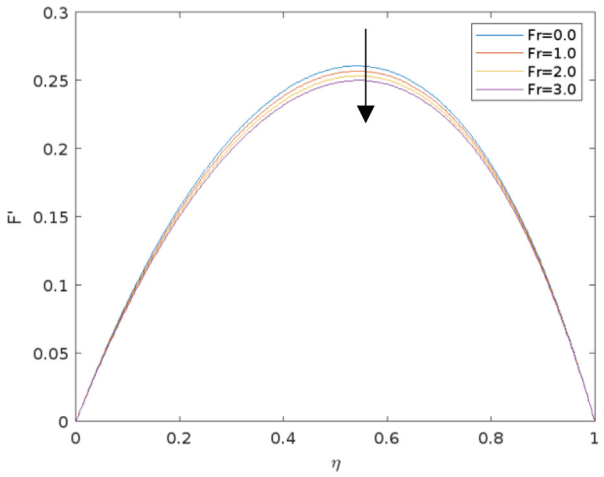

Fig. 3c Radial velocity VS Darcy-Forchheimer parameter.

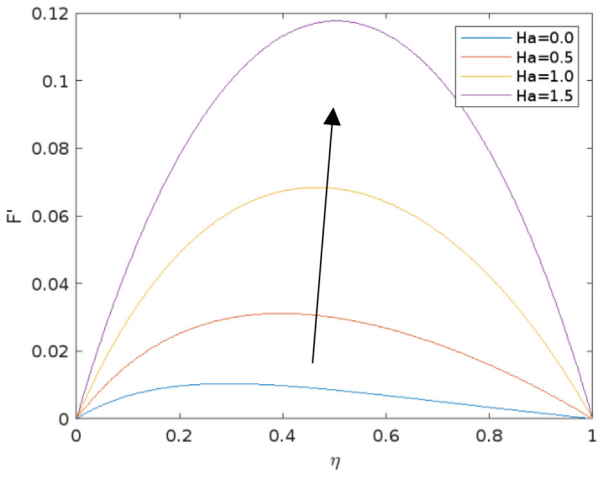

Fig. 3e Radial velocity VS Hartmann parameter.

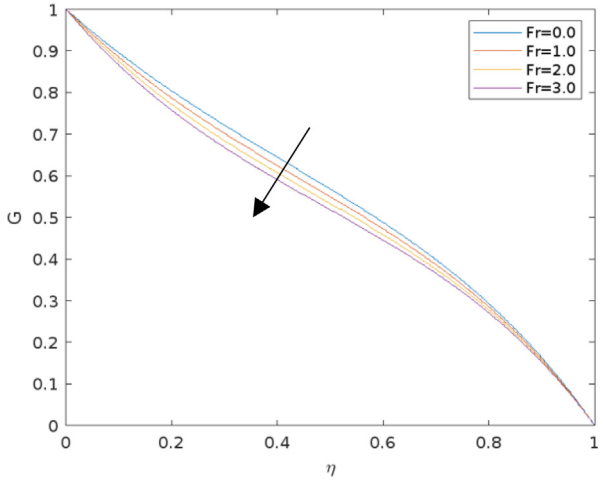

Fig. 3d Azimuthal velocity VS Darcy-Forchheimer parameter.

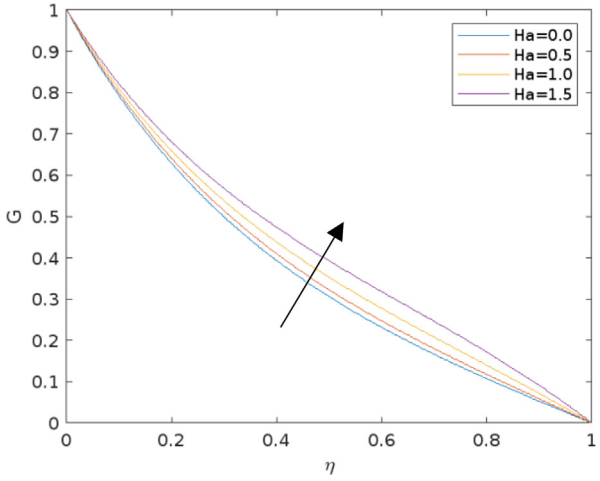

Fig. 3f Azimuthal velocity VS Hartmann parameter.

$$\left(\frac{k_{hnf}}{k_f}+1.33Rd\right)\theta'' + B_3\left[PrF\theta' + MBr\left(G^2+F'^2\right)+\frac{Br}{B_1B_2}\left(G'^2+F'^2\right)+PrNb\theta'\phi'+PrNt\theta'^2\right] = 0, \tag{12}$$

$$\phi'' + ScF\phi' + \frac{Nt}{Nb}\theta'' - ScKr\phi = 0 \tag{13}$$

Corresponding boundary conditions become:

$$\left.\begin{aligned} &F(\eta)=0, F'(\eta)=0, G(\eta)=1, \theta(\eta)=1, \phi(\eta)=1, at\eta=0\\ &F'(\eta)\to 0, G(\eta)\to 0, \theta(\eta)\to 0, \phi(\eta)\to 0, as\eta\to\infty \end{aligned}\right\} \tag{14}$$

Where,

$$\left.\begin{aligned} B1 &= [(1-\phi_1)(1-\phi_2)]^{2.5},\\ B2 &= \left[(1-\phi_1)+\phi_1\frac{\rho_1}{\rho_f}\right](1-\phi_2)+\phi_2\frac{\rho_2}{\rho_f},\\ B3 &= \left[(1-\phi_1)+\phi_1\frac{(\rho c_p)_1}{(\rho c_p)_f}\right](1-\phi_2)+\phi_2\frac{(\rho c_p)_2}{(\rho c_p)_f} \end{aligned}\right\} \tag{15}$$

The non-dimensional parameters used in Equations (10–13) are described as:

Porosity parameter:

$$\beta = \frac{v_f}{\omega k_0}$$

Magnetic parameter:

$$M = \frac{B_0^2\sigma_{hnf}}{\omega\rho_{hnf}}$$

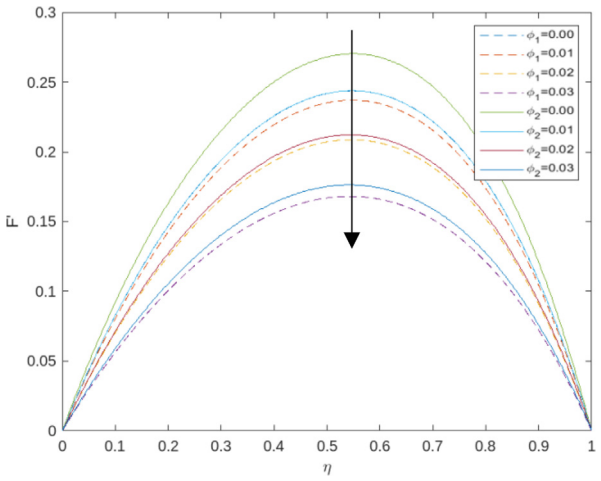

Fig. 3g Radial velocity VS Concentration parameter.

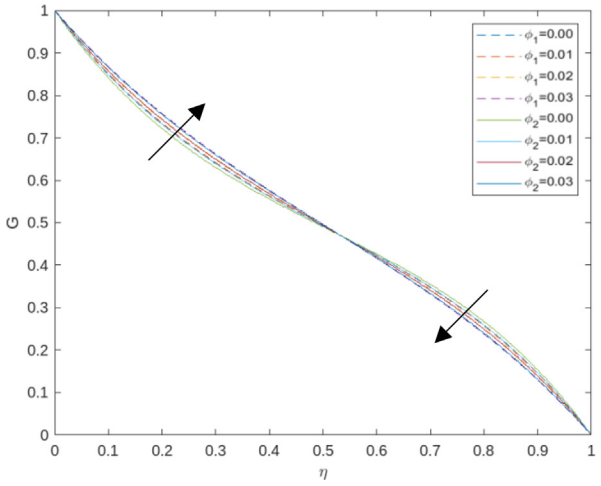

Fig. 3h Azimuthal velocity VS Concentration parameter.

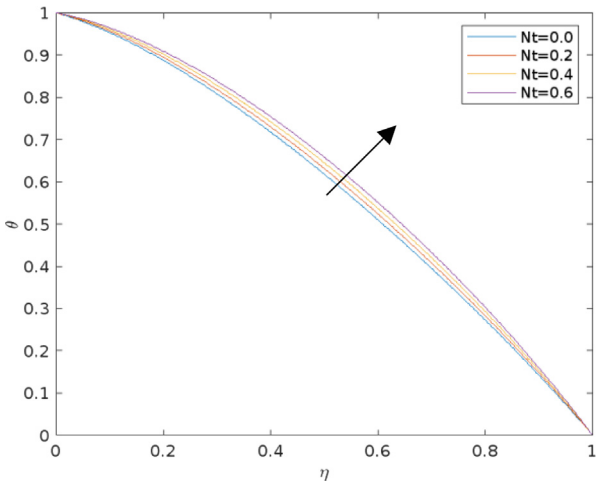

Fig. 4a Temperature VS Thermophoresis parameter.

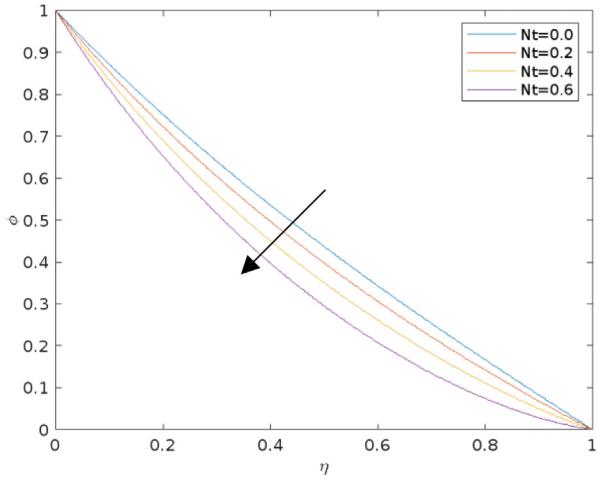

Fig. 4b Concentration VS Thermophoresis parameter.

Darcy-Forchheimer parameter:

$$Fr = \frac{C_b}{\sqrt{k_0}}$$

Hartmann number:

$$Ha = \frac{\pi}{8}\frac{j_0 M_0}{r\omega^2 \rho_f}$$

Radiation parameter:

$$Rd = \frac{4\sigma^* T_\infty^3}{k^* k_f}$$

Prandtl number:

$$Pr = \frac{v_f (\rho c_p)_f}{k_f}$$

Brinkman number:

Eckert number:

$$Ec = \frac{r^2\omega^2}{(T_f - T_\infty)(c_p)_{hnf}}$$

Width parameter:

$$\gamma = -\frac{\pi}{a_0\sqrt{\frac{\omega}{v_f}}}$$

Brownian motion parameter:

$$Nb = \frac{\tau D_B C_\infty}{v_f}$$

Thermophoresis parameter:

$$Nt = \frac{\tau D_T (T_f - T_\infty)}{T_\infty v_f}$$

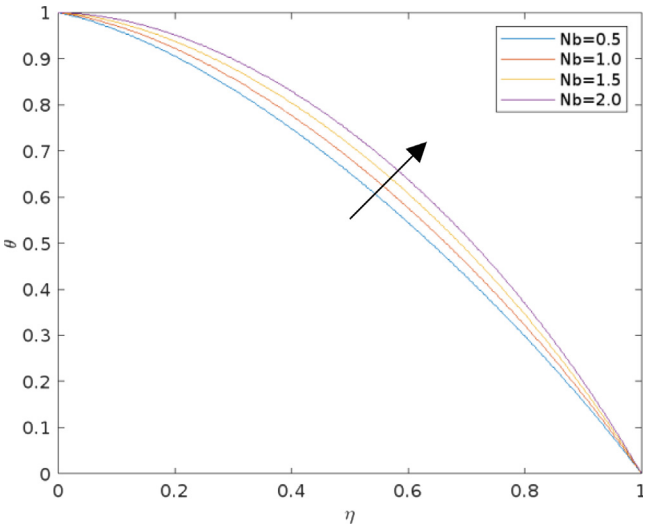

Fig. 4c Temperature VS Brownian motion parameter.

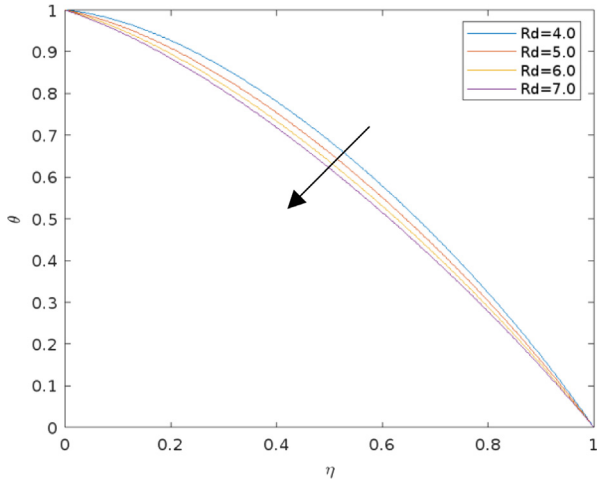

Fig. 4e Temperature VS Radiation parameter.

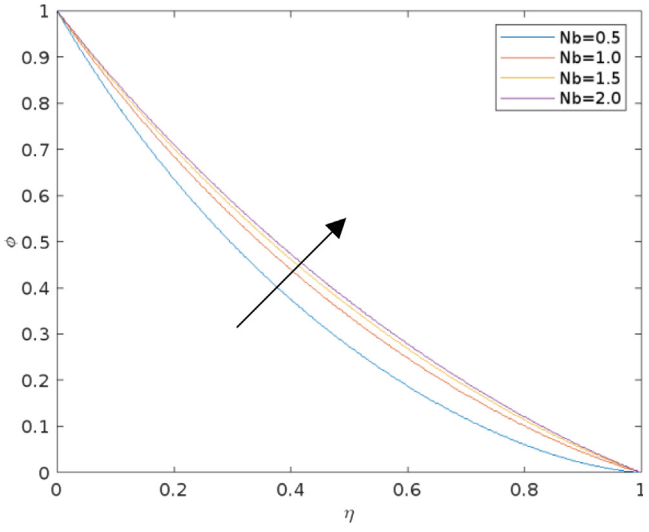

Fig. 4d Concentration VS Brownian motion parameter.

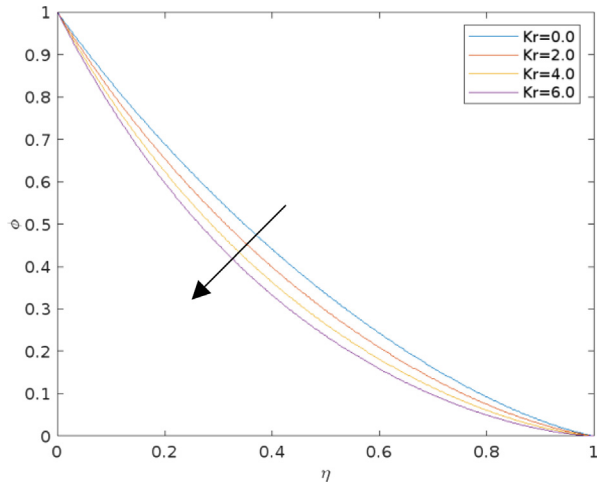

Fig. 4f Concentration VS Chemical reaction parameter.

Schmidt number:

$$Sc = \frac{v_f}{D_B}$$

Chemical reaction parameter:

$$Kr = \frac{k_r^2}{\omega}$$

Engineering quantities of Interests:

The physical quantities of interest like heat transfer rate, mass transfer rate, and skin friction coefficient are also analyzed in this study. The Nusselt number, skin friction coefficient, and Sherwood number are mathematically expressed as [63,64]:

$$Nu_x = \frac{r(q_w + q_r)}{k_f(T_f - T_\infty)}, C_f = \frac{\sqrt{\tau_W^2 + \tau_V^2}}{\rho_f U_w^2},$$
$$Sh_x = \frac{rm_w}{\rho_f D_B(C_f - C_\infty)} \quad (16)$$

Where, $(q_w + q_r)$ is the heat flux, τ_W is the radial stress, τ_V is the transverse shear stress, and m_w is the mass flux. They are defined as:

$q_w = -k_{hnf}\left(\frac{\partial T}{\partial z}\right)_{z=0}, q_r = -\frac{4.33T_\infty^3\sigma^*}{k^*}\left(\frac{\partial T}{\partial z}\right)_{z=0}, \tau_w = \mu_{hnf}\left(\frac{\partial W}{\partial z}\right)_{z=0}, \tau_V = \mu_{hnf}\left(\frac{\partial V}{\partial z}\right)_{z=0}, m_w = -\rho_f D_B\left(\frac{\partial C}{\partial z}\right)_{z=0}, Re_x = \frac{rU_w}{v_f}$ (Reynolds number) (17).

The non-dimensional form of above expressions are as follows:

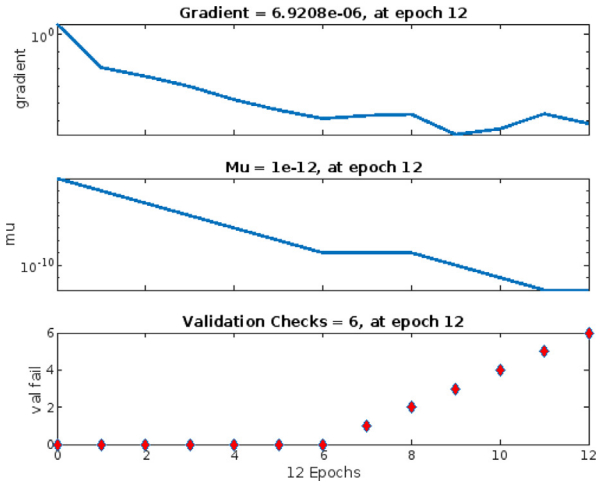

Fig. 5a Training state for Ha (Case-2).

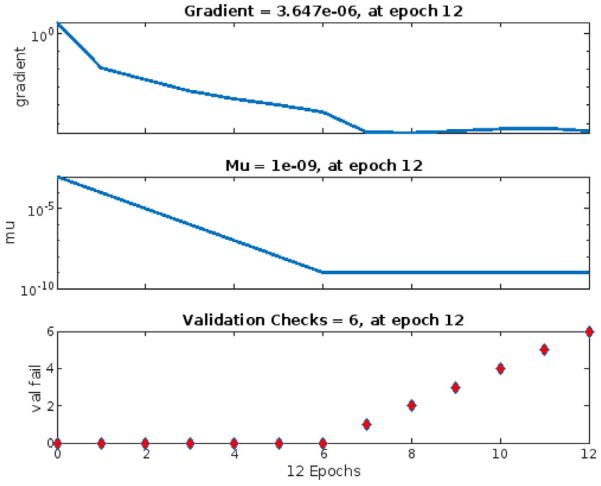

Fig. 5b Training state for Ha (Case-3).

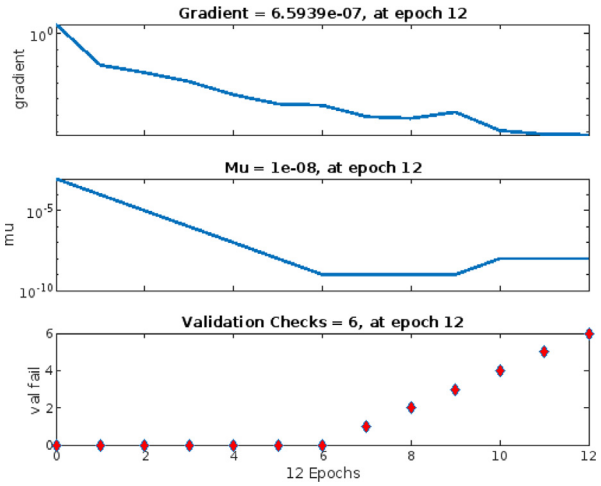

Fig. 5c Training state for Ha (Case-4).

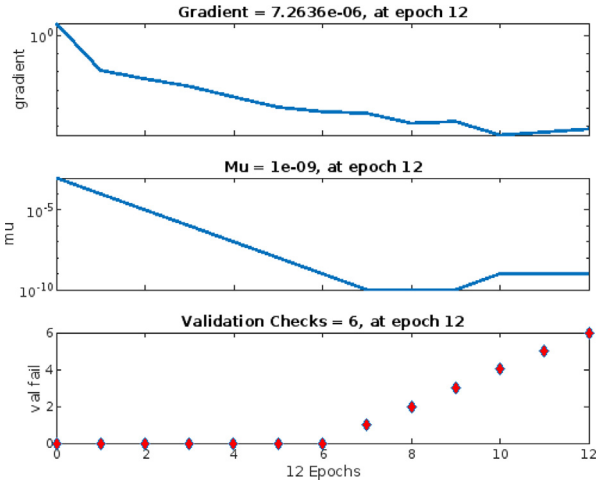

Fig. 5d Training state for Fr.

$$Nu_x Re_x^{-\frac{1}{2}} = -\left[\frac{k_{hnf}}{kf} + 1.33Rd\right]\theta'(0), C_f Re_x^{\frac{1}{2}} = \frac{\mu_{hnf}}{\mu_f}\sqrt{[F''(0)^2 + [G'(0)]^2}, Sh_x Re_x^{-\frac{1}{2}} = -\phi\prime(0) \quad (18)$$

3. Numerical solution

This section discusses a numerical methodology to obtain the solution of the nondimensional higher order coupled ODEs. For computational analysis, the Shooting procedure is a technique for solving a boundary value problem (BVP) by reducing it to an initial value problem (IVP) of first order differential equation. The obtained ODEs (10–13) and the boundary conditions (14) are treated by a convenient shooting method. Let us assume:

$$Y_1 = F;\ Y_2 = F';\ Y_3 = F'';\ Y_4 = G;\ Y_5 = G';$$
$$Y_6 = \theta;\ Y_7 = \theta';\ Y_7' = \xi\,(\text{Say});\ Y_8 = \phi;\ Y_9 = \phi' \quad (19)$$

The system of first-order differential equation is given by:

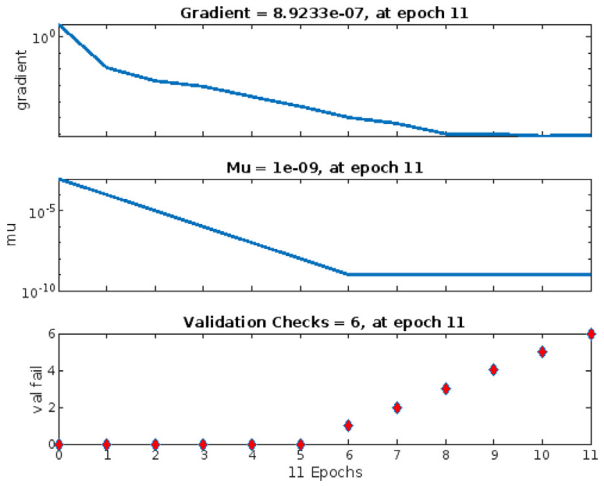

Fig. 5e Training state for Rd.

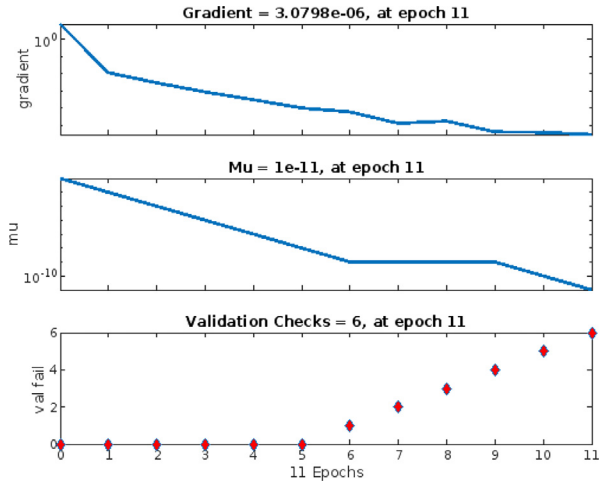

Fig. 5g Training state for Nt.

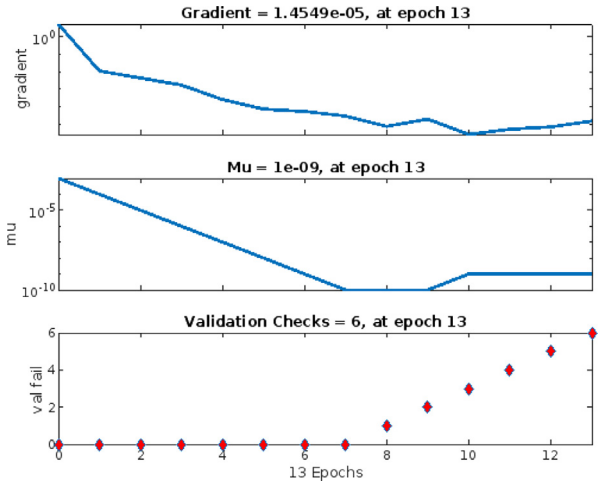

Fig. 5f Training state for Nb.

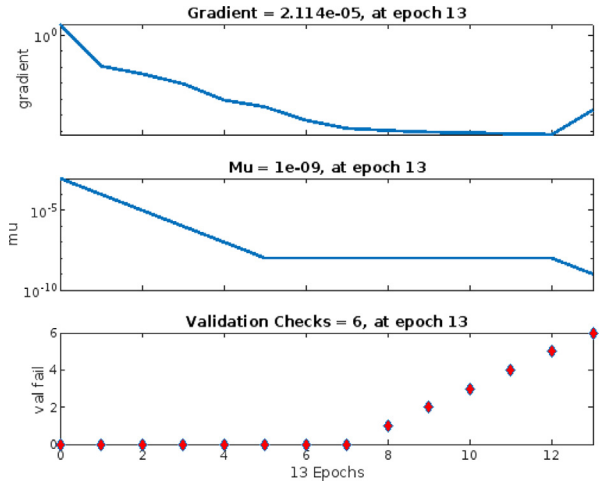

Fig. 5h Training state for Kr.

$$
\left.
\begin{aligned}
Y_1' &= Y \\
Y_2' &= Y_3 \\
Y_3' &= \beta Y_2 + B_1 B_2\left(Y_2^2 - Y_1 Y_3 - Y_4^2 + M Y_2^2 + Fr Y_2^2 - Hae^{\gamma\eta}\right) \\
Y_4' &= Y_5 \\
Y_5' &= \beta Y_4 + B_1 B_2\left(2 Y_2 Y_4 - Y_1 Y_5 + M Y_4 + Fr Y_4^2 - Hae^{\gamma\eta}\right) \\
Y_6' &= Y_7 \\
Y_7' &= \frac{-B_3\left[Pr Y_1 Y_7 + MBr\left(Y_4^2 + Y_2^2\right) + \frac{Br}{B_1 B_2}\left(Y_5^2 + Y_3^2\right) + Pr\delta Y_6 + PrNb Y_7 Y_9 + PrNt Y_7^2\right]}{\left(\frac{k_{hnf}}{k_f} + 1.33 Rd\right)} \\
Y_8' &= Y_9 \\
Y_9' &= ScKr Y_8 - ScF Y_9 - \frac{Nt}{Nb}\xi
\end{aligned}
\right\} \tag{20}
$$

and the corresponding boundary conditions become:

$$
\begin{aligned}
&Y_1(0) = 0;\ Y_2(0) = 0;\ Y_4(0) = 1;\ Y_6(0) = 1; \\
&Y_8(0) = 1;\ Y_2(\infty) = 0;\ Y_4(\infty) = 0;\ Y_6(\infty) = 0;\ Y_8(\infty) = 0
\end{aligned} \tag{21}
$$

4. Validation of the results:

This section validates the present results to previously published research work. Using the appropriate assumptions, the velocity and temperature profiles of the present work are compared to those of a prior study Ilyas et al. [20]. The present model is reduced to an already published work of Ilyas et al. [20]. Fig. 2a shows the F curve for a combination of dimensionless parameters, and Fig. 2b shows the temperature profile. From these figures, it is concluded that the results obtained in the current analysis are in good agreement with the study of

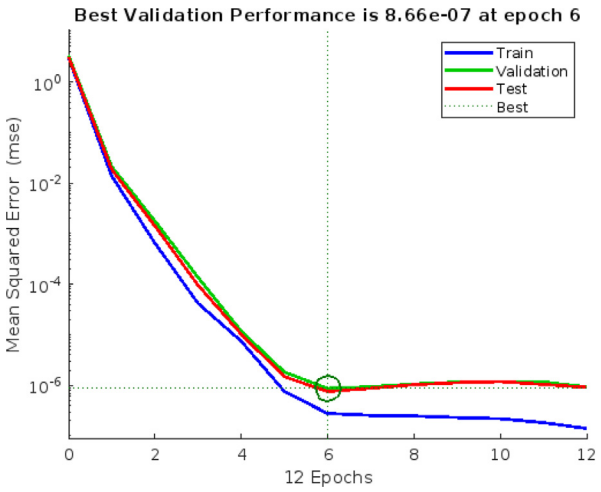

Fig. 6a Performance plot for Ha (Case-2).

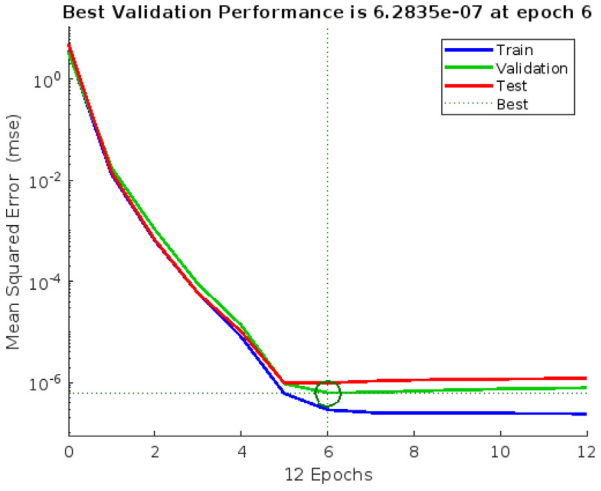

Fig. 6b Performance plot for Ha (Case-3).

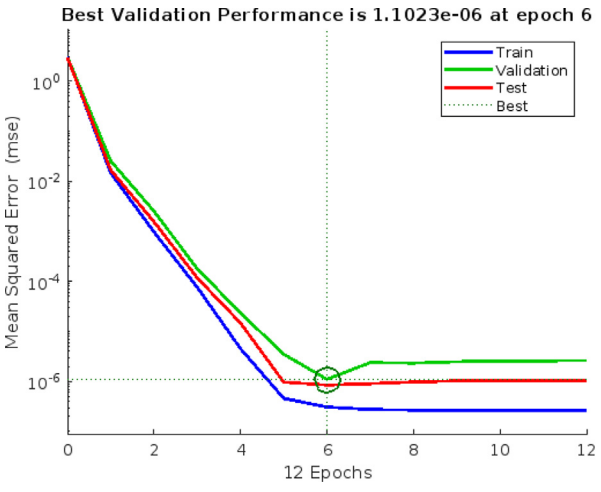

Fig. 6c Performance plot for Ha (Case-4).

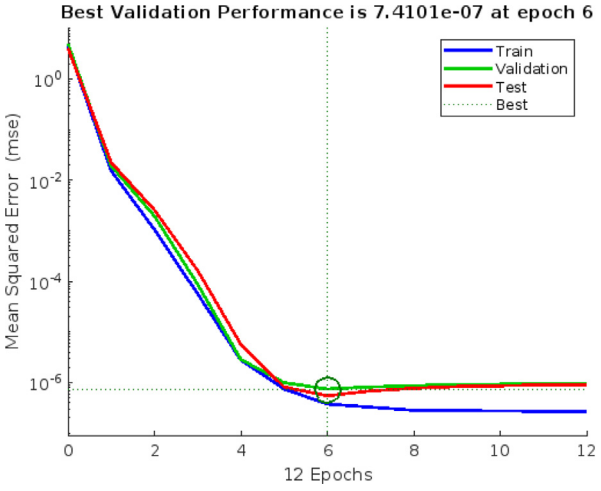

Fig. 6d Performance plot for Fr.

Ilyas et al. [20]. The comparative study can also be seen form Table 2. This section further contains details of the work of this study. Various plots of velocity, temperature, and concentration profiles were plotted for a combination of dimensionless parameters. The different cases and values of the physical parameters are shown in Table 3. Table 4 contains the reference and default values of flow parameters.

5. Solution design:

Levenberg-Marquardt's backpropagation algorithm is used to solve nonlinear least squares problems. It has increased convergence speed, avoids long training times, and it is often the fastest backpropagation algorithm in MATLAB. It interpolates between the Gauss-Newton algorithm and the gradient descent method. It often finds a solution, even if it starts far from the absolute minimum. This supervised algorithm solves by iteratively training the neural networks by backpropagation. Compared to the traditional methods, the algorithm is faster for well-behaved functions and reasonable starting parameters. For fine-tuning the weights, this method requires taking the error rate of forward propagation and feeding this loss backwards through the neural network layers. Using BVP5C in MATLAB, the ODEs (10–13), along with the boundary conditions, are solved. The present study considered 400 data points (η values) to evaluate obtained functions. This set of 400 data points is used as the input set for Levenberg-Marquardt's backpropagation algorithm. Fig. 2c represents the flow chart of the ANN methodology and solution with backpropagation solver. The algorithm steps are discussed below:

Input data: X-values are the η values, and Y-values are corresponding values of $F, Fl, G, [03B8]$, and ϕ.

1. **Initialization:** Input data is provided to the network for training, validation, and testing. Here, 90% (360 observations) are provided for training. 5% (20 observations) are provided for validation. 5% (20 observations) are provided for testing.

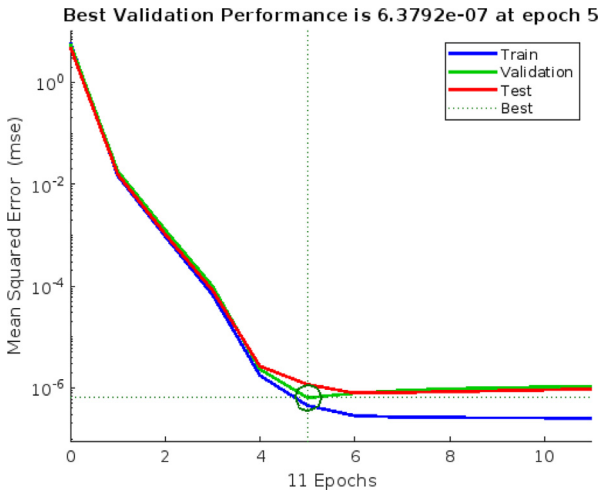

Fig. 6e Performance plot for Rd.

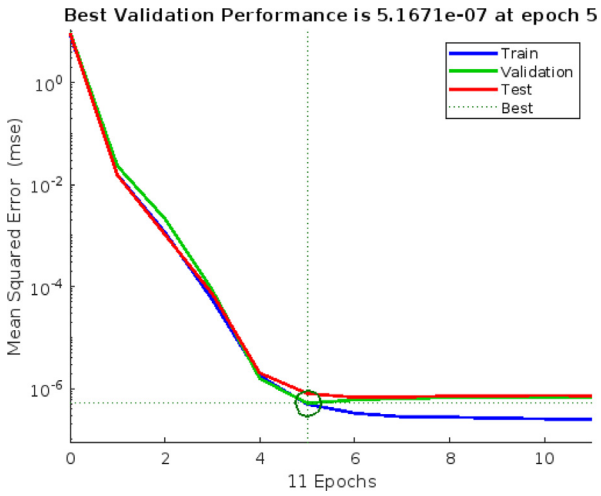

Fig. 6g Performance plot for Nt.

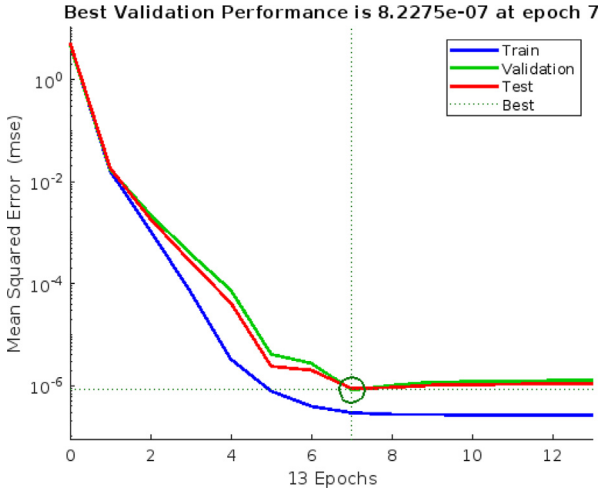

Fig. 6f Performance plot for Nb.

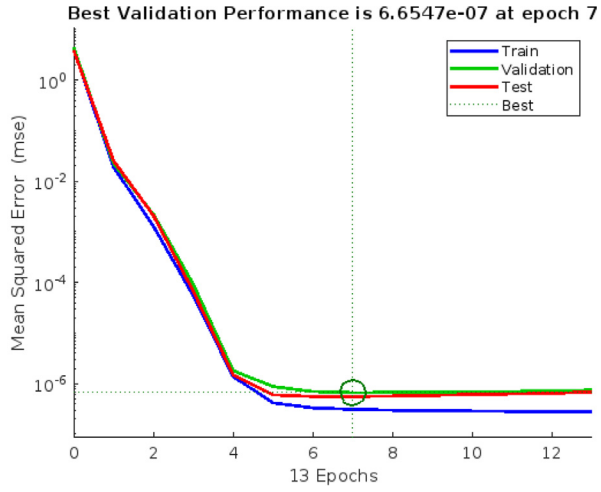

Fig. 6h Performance plot for Kr.

2. **Network design:** Values are assigned to network parameters like the number of neurons, number of delays, number of layers, etc. Here, 80 hidden layer network is considered.
3. **Training weights:** Network weights for the input data are trained through the Levenberg-Marquardt activation function.
4. **Stopping criteria:** Step 4 stops in the following conditions:

- The number of epochs (repetitions) has reached the limit.
- The time limit has been exceeded.
- Performance is minimal.
- The gradient of performance is less than the required minimum gradient.
- The algorithm Mu is greater than the given maximum Mu.
- Validation performance (validation error) increased more than maximum validation failures (when using validation).

5. **Testing:** The trained model is tested on the testing data. If a suitable network is not obtained, then repeat Step-2 and 3. Else, the network can be used for further investigation.

After training the LMBP model, it is analyzed using performance, network training, regression, error histograms, and fit plots. After solving the ODEs (10–13) using BVP5C, we get the functional solutions. After training the model, we have a trained model which incorporates those functions. These trained models can be directly used in many computer applications, can be integrated with mathematical software, and have much more importance. These models provide a simple and accurate way of predicting the fluid properties. The plots used for analysis provide useful information on the performance of various models. Depending on the requirements, the best model parameters can be obtained after studying these plots. Each plot has its own importance in the analysis, which is mentioned in the individual sections ahead.

6. Results and discussions

To get physical insight in to the problem, a combined effects of physical parameters; modified Hartmann number, ther-

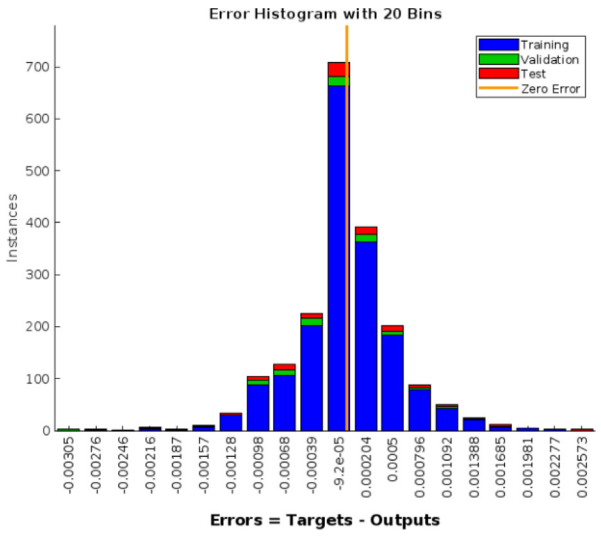

Fig. 7a Error Histogram for Ha (Case-2).

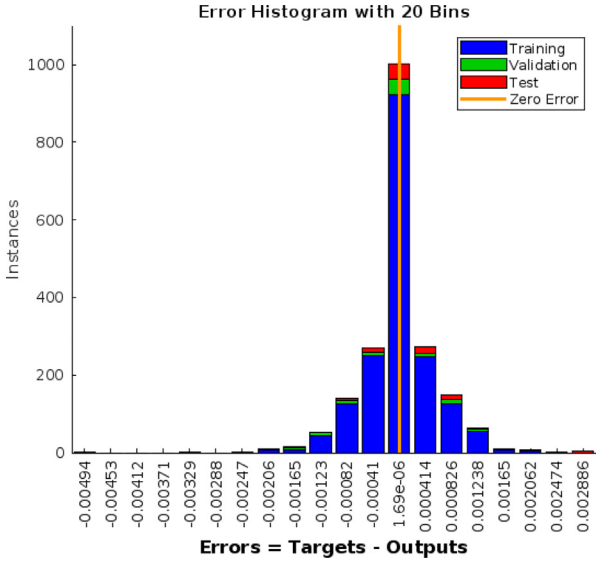

Fig. 7b Error Histogram for Ha (Case-3).

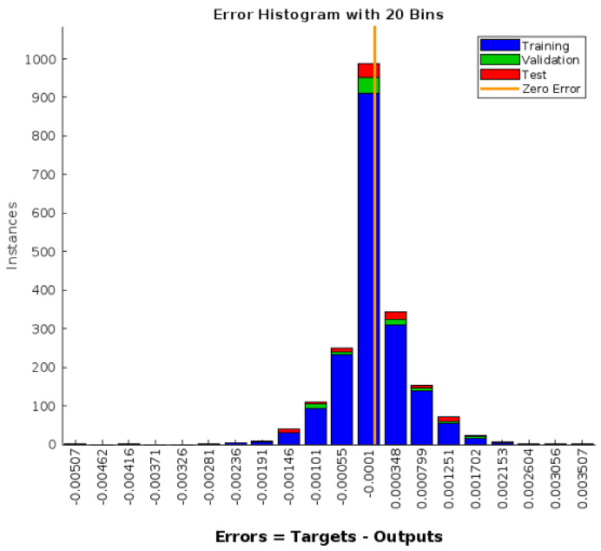

Fig. 7c Error Histogram for Ha (Case-4).

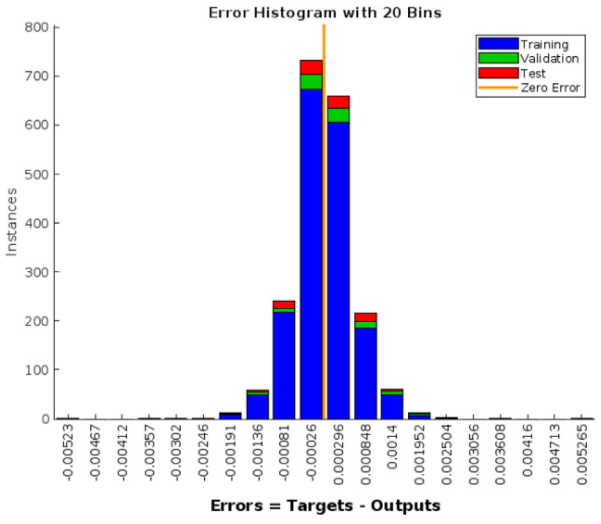

Fig. 7d Error Histogram for Fr.

mophoresis parameter, Brownian motion parameter, and chemical reaction parameter have been analyzed on velocity, temperature, and concentration profiles. The determination, designing, convergence, verification, and stability of the Levenberg-Marquardt backpropagation neural network algorithm are validated on the assessment of achieved accuracy through performance, fit, regression, and error histogram plots for the discussed hybrid nanofluid. Physical quantities of engineering interest like heat transfer rate, mass transfer rate, skin friction coefficient are also discussed in this study.

6.1. Velocity profile

Figs. 3a–3h illustrate the behavior of velocity profiles by changing the values of physical parameters $M, Fr, Ha, \phi_1, and \phi_2$. Figs. 3a and 3b reveal that by increasing the values of magnetic field parameter M, the velocity profile decrease. Physically, larger values of M generate stronger Lorentz force that eventually decreases the velocities. Also, the viscosity of porous medium increases by increasing M, this enhances the viscosity of the hybrid nanofluid. Fluid velocity through a porous medium is inversely proportional to the viscosity, hence the velocities of the hybrid nanofluid decreases. Figs. 3c and 3d show that as increasing the value of Darcy-Forchheimer parameter Fr, the velocity profile decrease. Physically, the drag force increases on increasing Fr, as it is directly proportional to the inertia. Hence decreasing effect can be seen in velocity profile due to increase in quadratic drag forces. Figs. 3e and 3f illustrate that increasing the value of Hartmann parameter Ha, the radial velocity is drastically increases and azimuthal velocity also shows an improvement, especially at $\eta = 0.1$. This is because, by increasing Ha, the magnetic field applied on the Riga plate increases, which increases the Lorentz force in the direction of fluid flow. The combined effect of magnetic and Lorentz force sufficiently enhances the veloc-

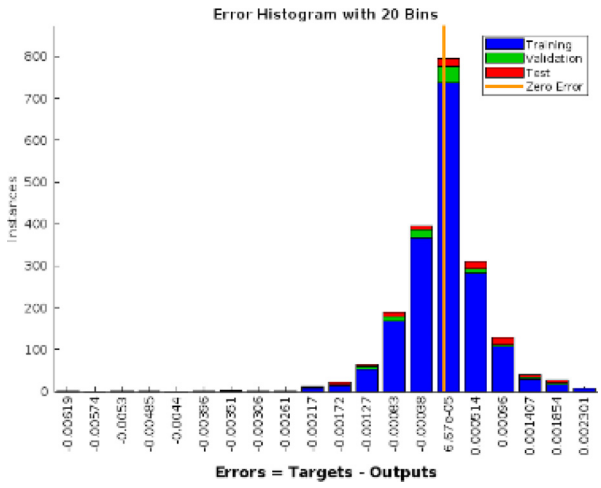

Fig. 7e Error Histogram for Rd.

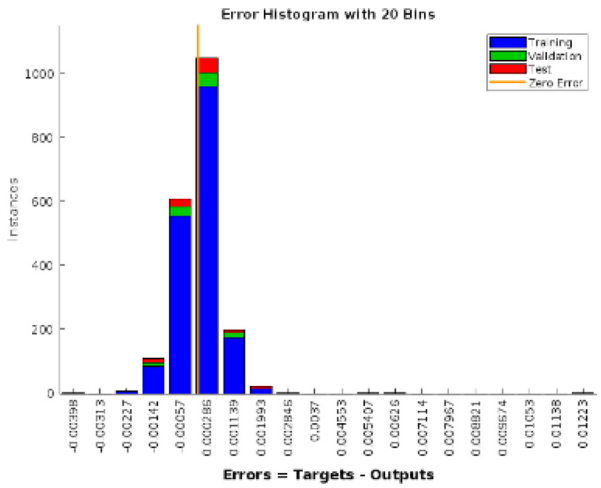

Fig. 7g Error Histogram for Nt.

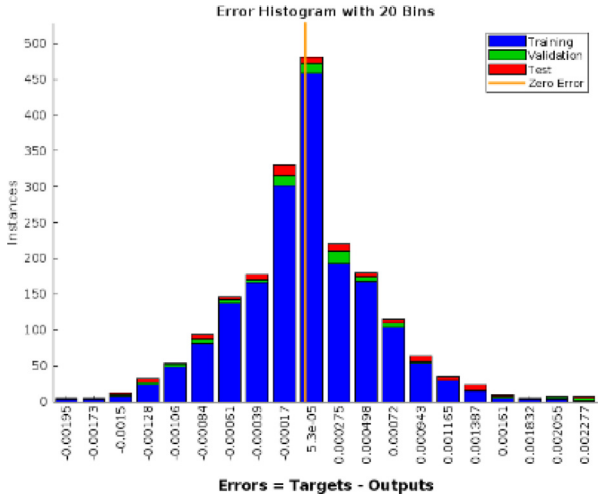

Fig. 7f Error Histogram for Nb.

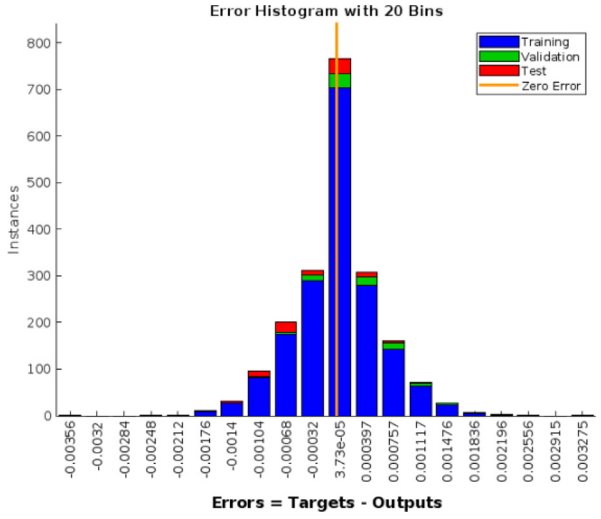

Fig. 7h Error Histogram for Kr.

ities. Figs. 3g and 3h depict the effect of concentration of Al_2O_3 (ϕ_1)and concentration of Ag (ϕ_2) on the velocity profile. It is observed that fluid velocity decreases by increasing concentration of nanoparticles. The decrease in fluid velocity can be justified as, on enhancing the quantities of nanoparticles in the base fluid, the fluid feels resistance for its motion. From Fig. 3g, the radial velocity decreasing by increasing the concentrations of nanoparticles. There is a decrease in azimuthal velocity also, but not as much as radial velocity. The velocity of fluid is increasing till $\eta \approx 0.5$, this might be because a greater number of particles can now carry the energy for fluid movements.

6.2. Temperature and concentration profile

Figs. 4a–4f shows the effect of Nb, Nt, Rd, and Kr on temperature and concentration profiles. Figs. 4a and 4b illustrate that by increasing the thermophoresis parameter Nt, the temperature increases and hence the concentration decreases. Physically, the particles close to a hot surface produce more thermophoretic force. Thermophoretic force is the transport force that occurs due to the presence of a temperature gradient. When Nt is increases, the temperature gradient increases and hence the temperature profile enhances. Also from Fig. 4b, by increasing Nt, the temperature of boundary layer increases, it moves particles away from the surfaces within the base fluid. As a result, solute particle deposition away from the surface rises, causing concentration profile to decrease. Figs. 4c and 4d illustrate the effect of Brownian motion parameter Nb, on temperature and concentration profiles. Brownian motion is the random movement of suspended particles in the base fluid. It gets impacted by the fluid's quickly moving atoms or molecules. Fig. 4c shows on increasing Nb, the temperature increases. Physically, enhanced Nb increases the random and rapid motion of nanoparticles in the base fluid. This increases the random collisions of the nanoparticles within the fluid. The greater the number of collisions, the more heat is generated. Fig. 4d depicts on increasing Nb, the concentration increases.

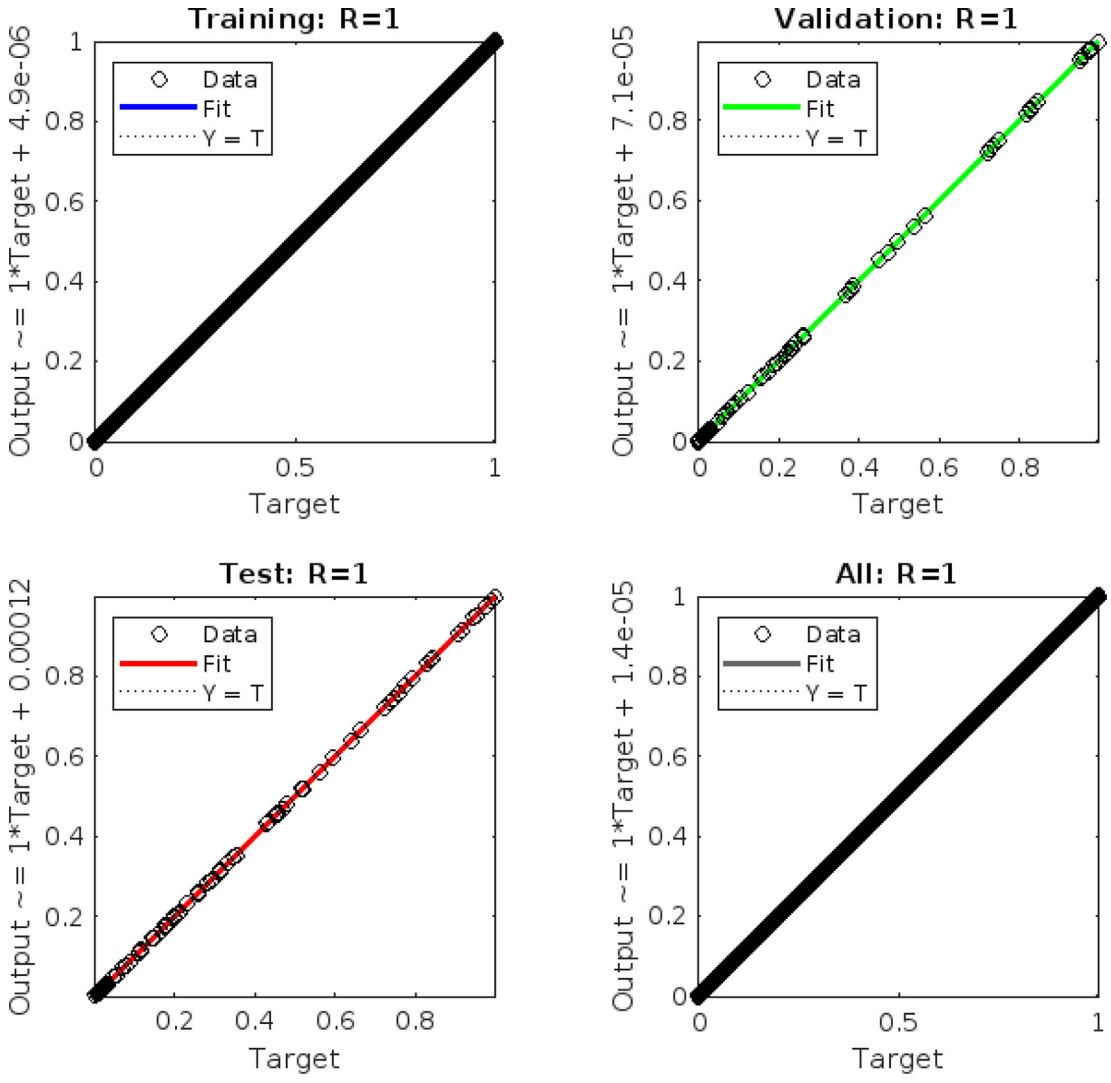

Fig. 8a Regression plots for Ha (Case-2).

Physically, as the random motion of particles enhances, the collisions of nanoparticles with each other increases the rate of chemical reaction. This faster chemical reaction increases the fluid concentration. Also, the generated heat energy helps to reduce the reaction's activation energy barrier. From the figure, it can be seen that the concentration increases more when Nb is changed from 0.5 to 1.0 and then the magnitude of the change decreases eventually. Fig. 4e shows the effect of radiation parameter on thermal profile. The figure shows that on increasing Rd, the temperature profile decreases. Physically, greater values of Rd show a more dominant effect over conduction. Radiations release a good amount of heat in the system which raises the outside temperature, reducing the fluid temperature due to temperature difference. Fig. 4f represents the effect of chemical reaction parameter, Kr on the concentration. The figure shows that by increasing Kr the concentration profiles decrease. The collisions between the nanoparticles enhance within the fluid near the surface for enhanced Kr. This eventually reduces the concentration of the hybrid nanofluid and boundary layer thickness.

6.3. Training state plots

Figure 5 shows the training state plots for the trained ANN. Training state plots are essential as they give us crucial information about the obtained model, like gradient, mu, optimal epochs, and how it reached the optimal state. For the convergence of the model, mean squared error (MSE) is used here. MSE is obtained by taking the mean of the squared difference of output or values predicted by ANN and targets or actual values. There is a pre-decided MSE for each epoch of the model. If the MSE value of any epoch crosses that value, the model considers it a validation failure. By default, the model takes six validation failures as the stopping condition. Figure 5 shows that the model stops the training after six validation failures and gives the optimal ANN model. The gradient is the logarithmic value of the backpropagation gradient for each iteration. It indicates that the model has hit the local minimum of objective function at its lowest point. The neural network training algorithm's control parameter is called mu. Choosing

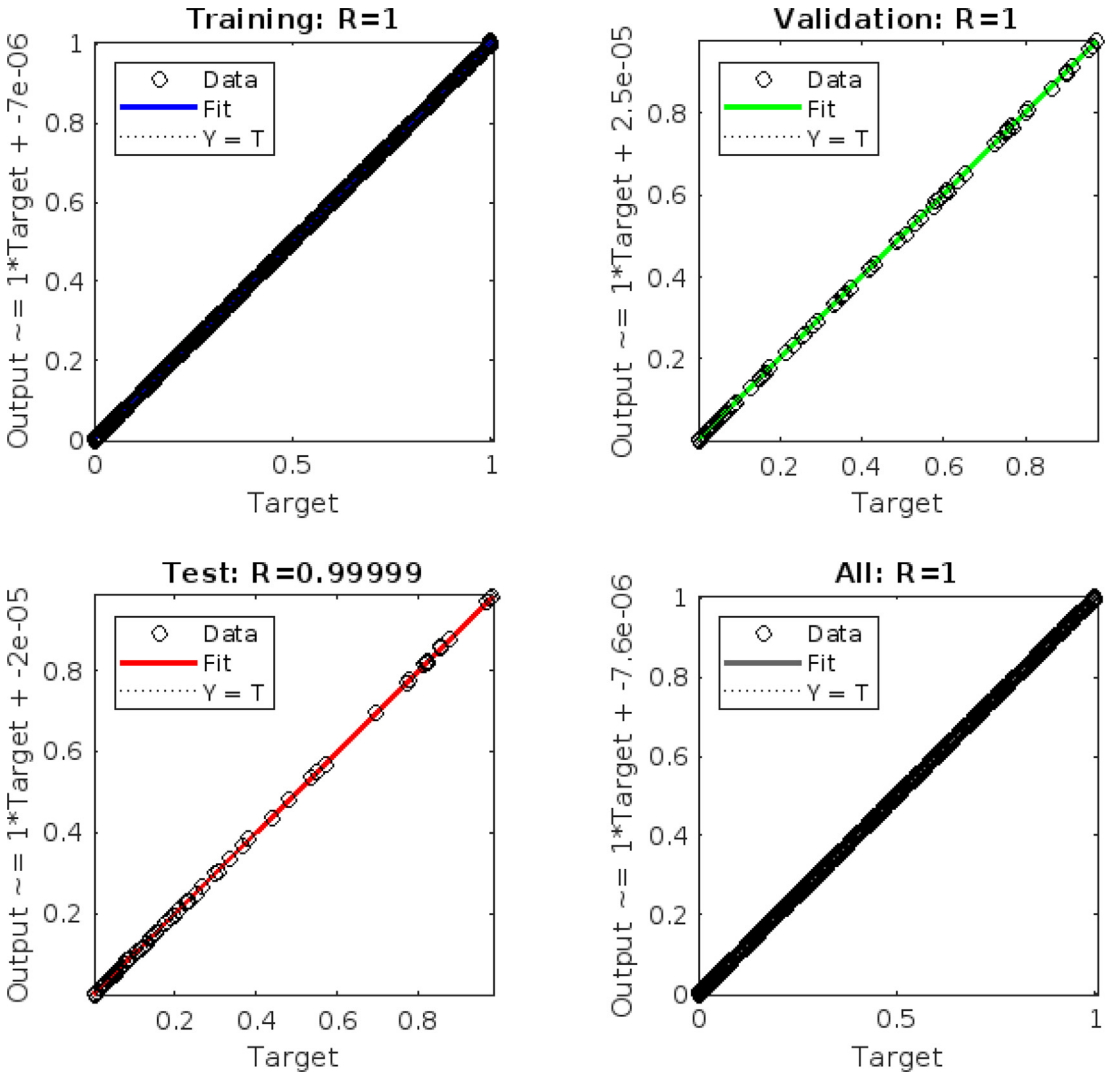

Fig. 8b Regression plots for Ha (Case-3).

mu has a direct impact on the convergence of errors. Fig. 5a shows that the ANN for Case-2 of Ha (i.e., Ha = 0.5) has converged at epoch 12. At epoch 12, it has a gradient of 6.92E-06 and mu of 1.00E-12. It can also be seen that after epoch six, it saw six validation failures and stopped the training. Fig. 5b shows the final ANN has a gradient of 3.65E-06 and a mu value of 1.00E-09. It saw six validation failures after epoch six and achieved epoch 12 as an optimal epoch. Fig. 5c shows the model has a gradient of 6.59E-07, a mu value of 1.00E-08, and 12 as the optimal epoch. Figs. 5d–5h can similarly be interpreted. Most of the ANN's training stopped at the 12th epoch. Some also have the 11th and 13th epochs. This also shows that the data was similar in nature.

6.4. Performance plots

Figure 6 shows the validation performance plots. These plots are obtained when the model is tested on the validation dataset simultaneously after each epoch to tune the network weights. The validation failure numbers can also be verified from these plots. When the model starts the training on the training data, in the starting epochs, the MSEs are very high on all three datasets. The errors start decreasing when the model begins moving toward the optimal state. The plots also show the best validation performance in dotted lines. This line corresponds to the best performance of the model in the validation phase. However, in all the graphs, the validation error increases after the best-fit line. Along with validation errors, the testing error is also increasing for each next epoch. In contrast, the training error is decreasing. This validates the hypothesis of overfitting. When the model is trained on a lot of training data, it becomes overfitted and performs poorly on validation and test data. From Fig. 6a, the validation performance of the model was very high from epoch 0 to 6. At the 6th epoch, it gave the best validation performance, with an MSE of 8.66E-07. However, the model did not stop the training at this epoch, as the training error decreased. After six validation failures or for six more MSEs, more than the best performance MSE will be allowed. After that, the model would reach convergence. Fig. 6b shows that the best validation performance was achieved at epoch 6 with an MSE of 6.28E-07. After six validation failures, it stopped the training at epoch 12. The training error decreases

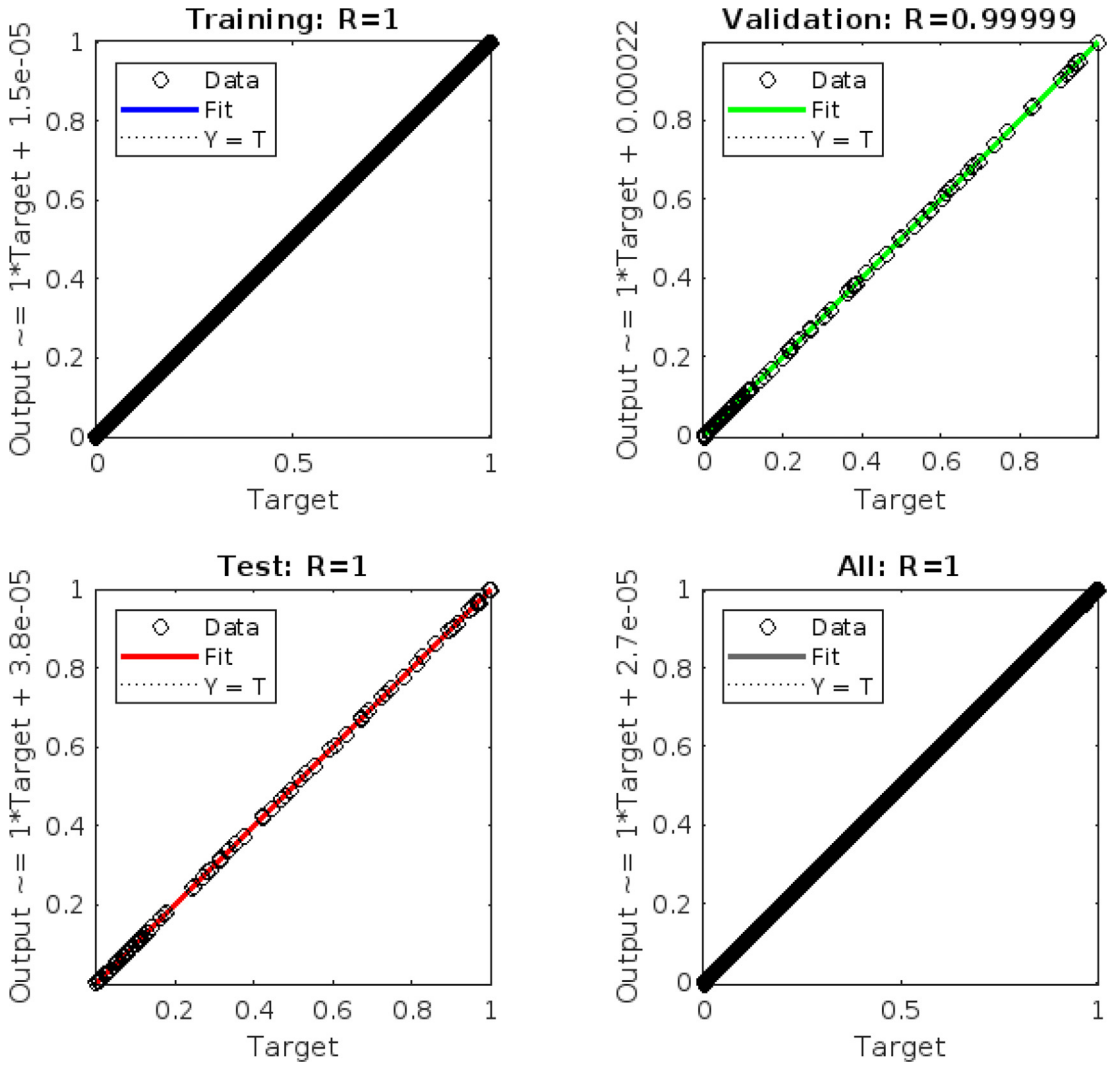

Fig. 8c Regression plots for Ha (Case-4).

after the best performance, and testing and validation errors remain the same. Fig. 6c shows the best performance of 1.10E-06 at epoch 6. The training and testing errors almost became straight lines, whereas validation errors became straight after the 7th epoch. A similar trend can be observed from Figs. 6d–6h. From all the plots, it can be concluded that the models converged with lower values of all three errors.

6.5. Error Histogram

Figure 7 shows the error histograms. As the whole data was divided into training (90%), validation (5%), and testing (5%) datasets. From all these three datasets, sampling is performed. Many samples are obtained, and the model is used on each sample to predict the output and then compared with the target or actual values. Errors are calculated for each sample. Those errors are categorized into 20 bins. All those 20 bins are plotted along with the number of samples constituting those errors. Figure 7 shows that the X-axis represents the error bins, Y-axis represents the instance the error occurred or the number of samples that has an error in that bin. The orange-colored zero lines represent zero error. Fig. 7a shows that from training data, around 650 samples has errors almost 0. From validation data, around 20 samples had zero errors, and from testing data, around 30 samples had zero errors. Hence, most samples has zero error from all three datasets. Fig. 7b illustrates that around 850 samples from training data has zero error, and about 50 from validation and testing has zero error. Fig. 7c shows 920 samples has zero error, and around 50 from the other two data has zero error. Similarly, Figs. 7d, 7e, 7f, 7g and 7h can be interpreted. From all these plots, most of the samples from the three datasets has zero errors. Hence, all the obtained ANNs are well-trained.

6.6. Regression plots

Figure 8 shows the linear regression plots. These plots are obtained when the trained ANN is used on all training, validation, and testing data to make the prediction, and then the predicted values are compared with the actual values. The outputs and targets form a linear relationship that would decide the model's goodness. It follows an equation of output = R * target + bias. If R = 1, then the model is working nicely. If R = 0, then the model has completely failed. Figure 8 shows

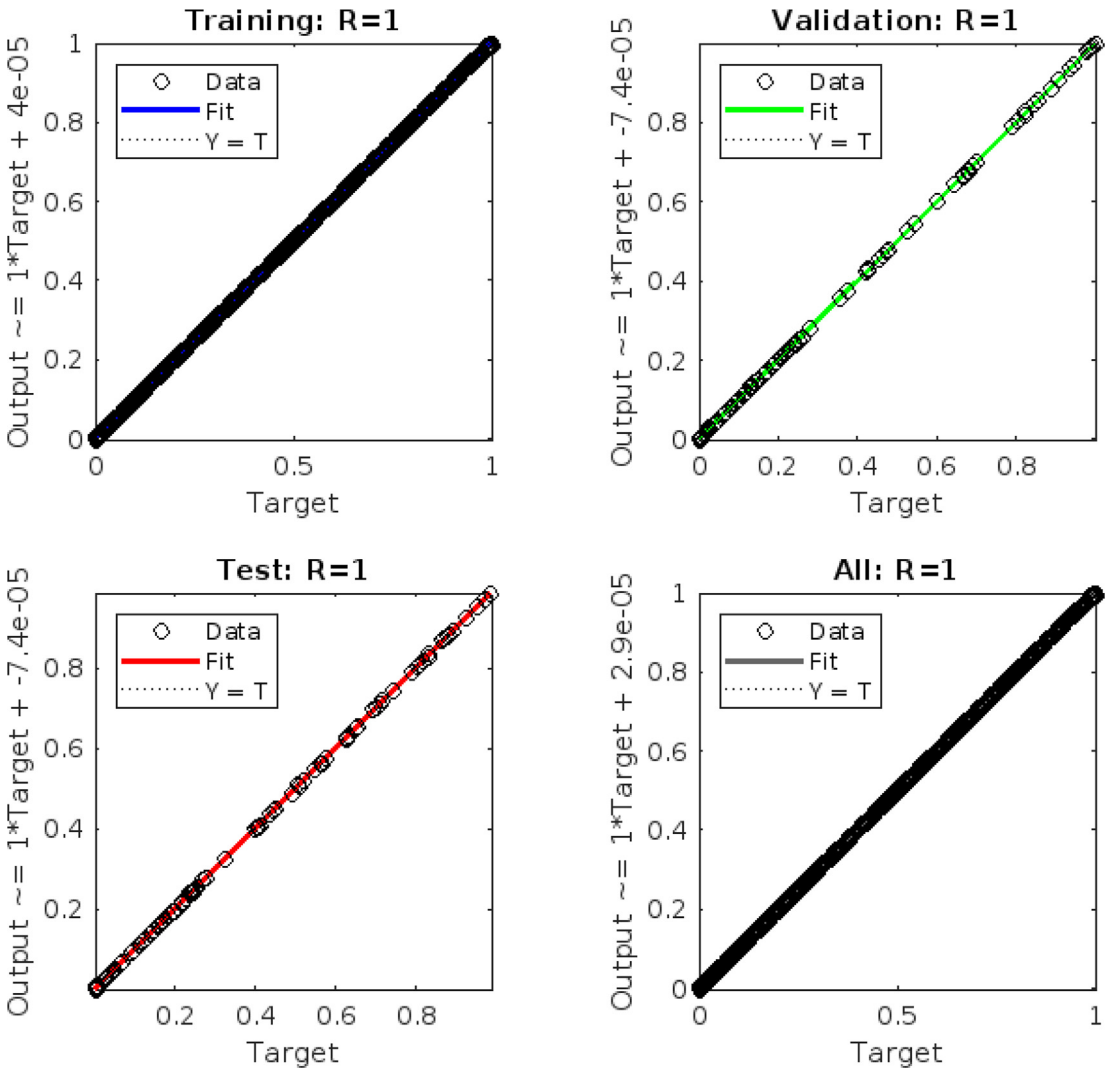

Fig. 8d Regression plots for Fr.

that most regression plots have R = 1 in full, training, validation, and testing datasets. That means that all the obtained ANNs are working excellently. The training data was obtained using the functions for F, F', G, θ, and ϕ for η values between 0 and 1. The network just incorporated the function into the weights. Predicting values from the neural network or the solutions obtained from BVP5C would give almost the same results. However, the neural network is essential, as it has incorporated all those functions into one model. From an applications point of view, the ANNs can be used in many fields rather than just a simple function. From Fig. 8a, when the model gave R = 1 for all four datasets. The output is almost the same as the target. The bias is, however, different in all four cases. Fig. 8b shows training data has R = 0.99999. Still, it is perfect accuracy. The other datasets show R = 1 which is the biases in all four are different. In Fig. 8c, the validation data gave R different form 1. But the model still performed almost best on all datasets. Similarly, Figs. 8d, 8e, 8f, 8g and 8h can be interpreted. Overall, it can be concluded that the ANNs gives excellent results for regression analysis.

6.7. Fit plots

Figure 9 shows the fit plot for the ANN model for considered problem. The fit plots are obtained using the trained ANN to predict the values from training, validation, and testing data and then comparing with the actual values. In the graphs, blue represents the training data, green represents the validation data, and red represents the testing data. The orange line represents the errors between the target and output values. The black line corresponds to the best fit of the model. The below plot shows the zoomed view of errors. The X-axis is between 0 to 1, representing the values of η. The figure illustrates the axial velocity predictions by the model. Fig. 9a shows that the model predicted the axial velocity in accordance with the output. The outputs and targets match with each other. There can be a slight deviation seen in the first lower part of the values. The model gave large enough errors throughout the η values of 0 to 1. Fig. 9b shows aroundη = 0.4, the model gave errors. Otherwise, it was the almost best fit. The outputs and targets match with each other well. The large error shown in the error

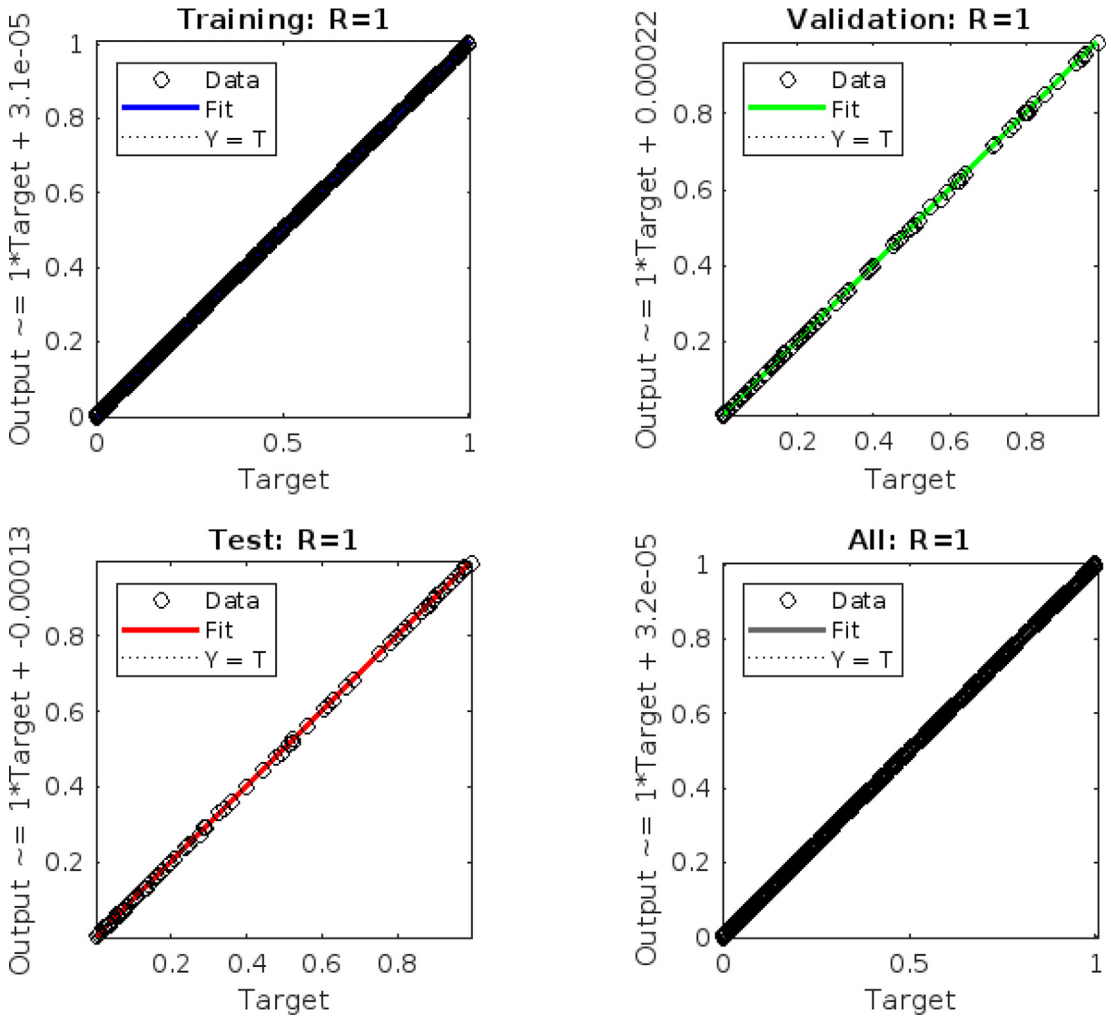

Fig. 8e Regression plots for Rd.

plot is not much visible in the plot. The starting values and ending values are in good agreement with each other. The mid values may see some lower jumps for outputs. Fig. 9c depicts that the algorithm predicted the outputs well with the targets. It can be inferred from the figure that with respect to the earlier two models, the model gave slight variations for all the η values, but not much larger deviations and errors were seen. However, significant errors at$\eta = 0$ and$\eta = 1$ can be seen in the plot. Similar behavior is observed from Figs. 9d, 9e, 9f, 9g and 9h. Overall, all the plots have shown lesser error. Hence, the models were the best fit for the data. Now, Table 5 shows the complete analysis of NN-LMBP based on validation, testing and training datasets for all the scenarios shown in Table35.

6.8. Engineering quantities of physical interest

Figure 10 shows the contour plots of quantities of physical interest. The contour plots can determine the desired response values and operating conditions. Fig. 10a shows the contour plot for heat transfer rate along with Nt and Nb. It is observed that by increasing the values of Nt and Nb, the heat transfer rate is decreasing. Fig. 10b depicts that by increasing the value of Rd, the thermal radiation would increase, resulting the increment in heat transfer rate. The effect of heat radiation improves the conduction properties of the nanofluid. This happens because more heat will generate, which will enhance the thickness of the thermal boundary layer. Further, by increasing the value of M, the heat transfer rate decreases. Fig. 10c

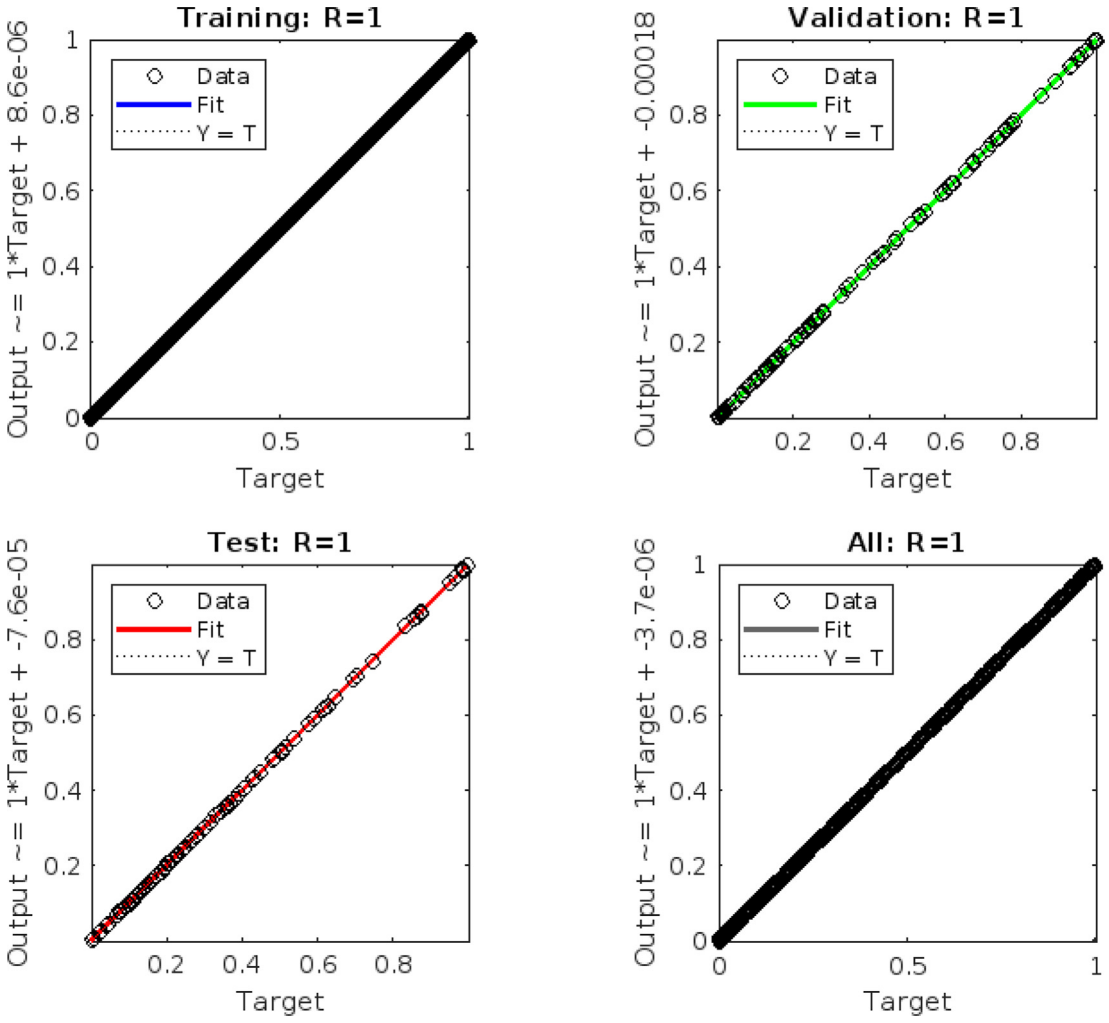

Fig. 8f Regression plots for Nb.

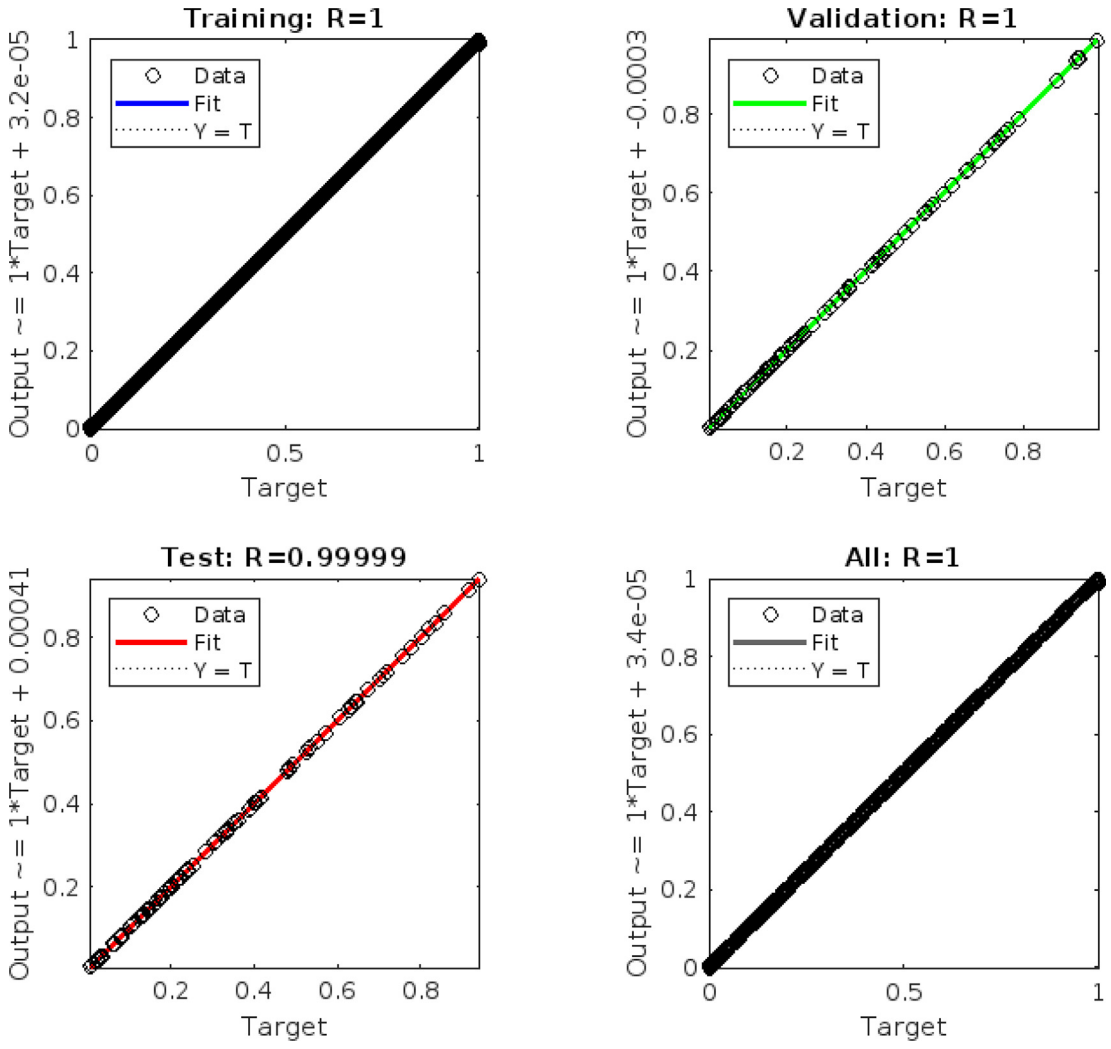

Fig. 8g Regression plots for Nt.

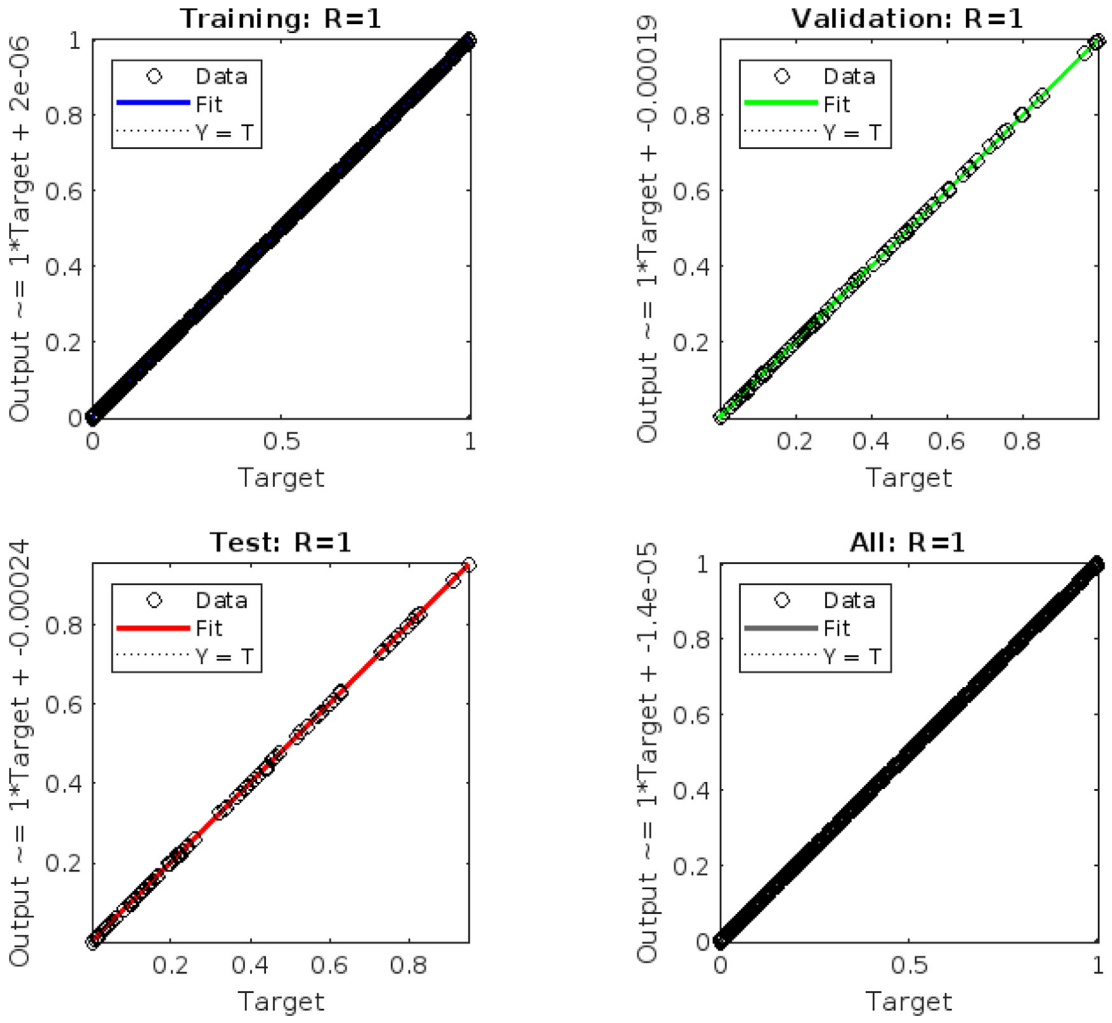

Fig. 8h Regression plots for Kr.

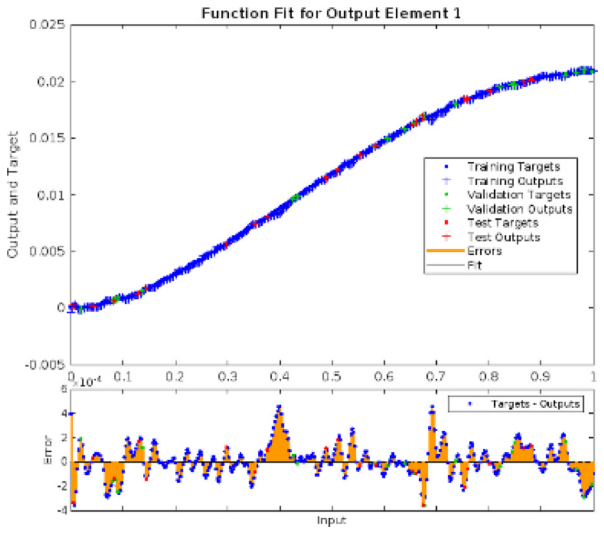

Fig. 9a Fit plots for Ha (Case-2).

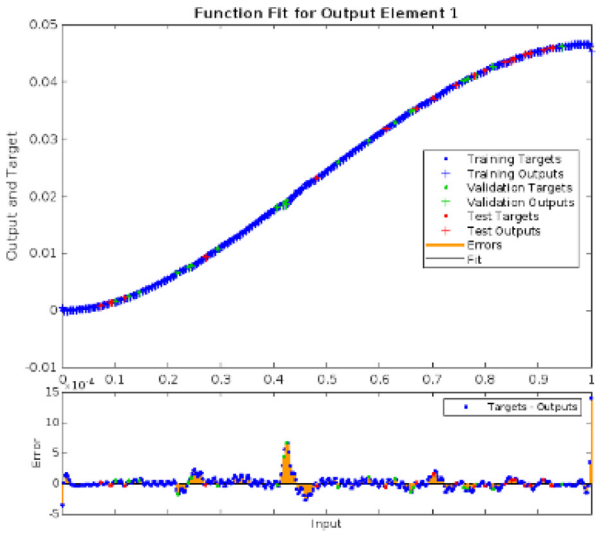

Fig. 9b Fit plots for Ha (Case-3).

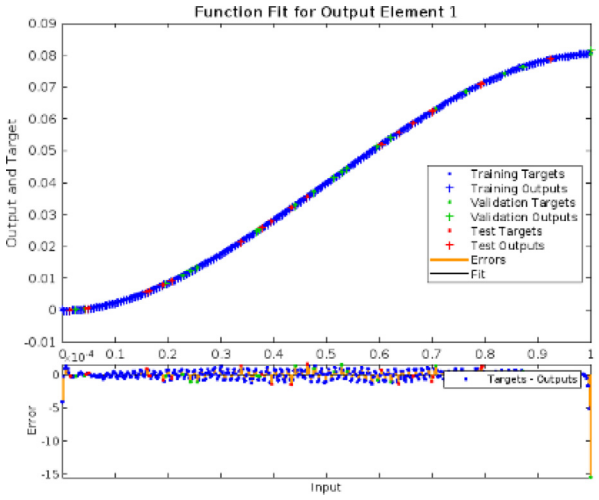

Fig. 9c Fit plots for Ha (Case-4).

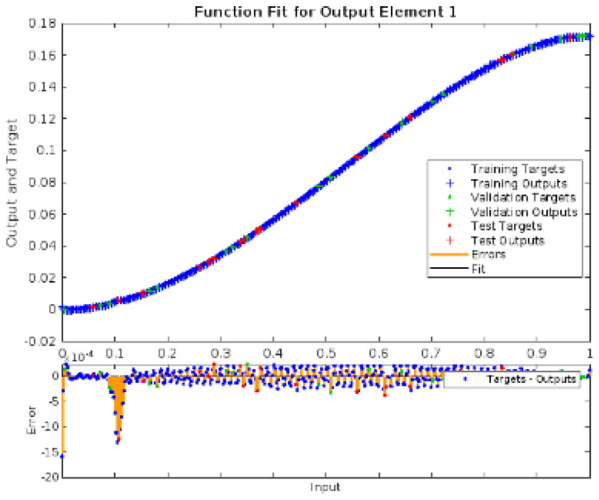

Fig. 9d Fit plots for Fr.

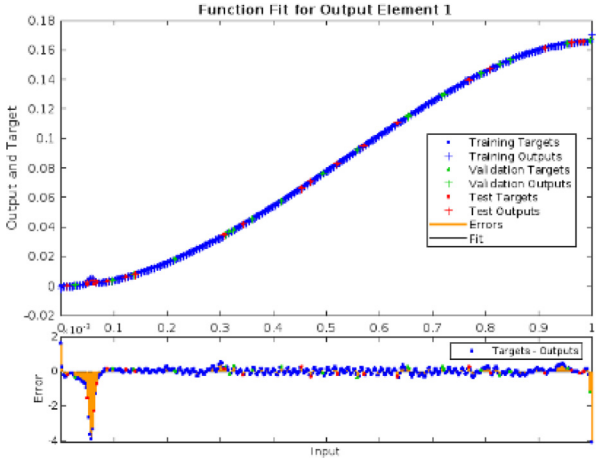

Fig. 9e Fit plots for Rd.

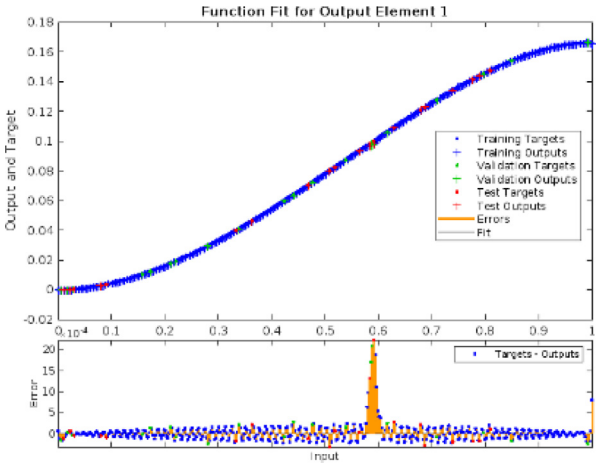

Fig. 9f Fit plots for Nb.

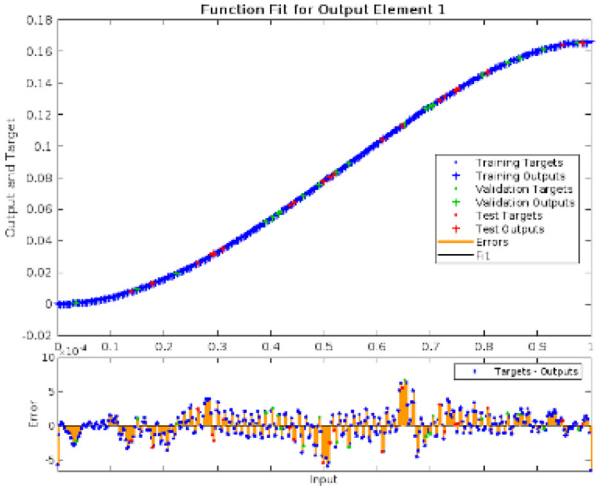

Fig. 9g Fit plots for Nt.

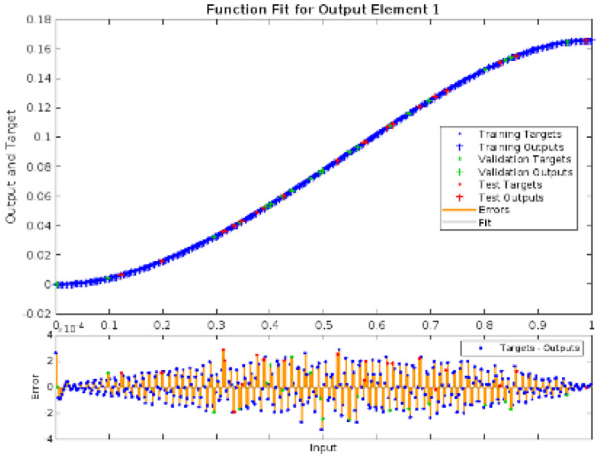

Fig. 9h Fit plots for Kr.

Table 5 Complete analysis of NN-LMBP based on validation, testing and training.

P.	Cases	Time(sec)	MSE			Perform-ance	Gradient	Mu	Epochs
			Training	Validation	Testing				
Ha	1	8	2.77E-07	8.66E-07	7.53E-07	1.40E-07	6.92E-06	1.00E-12	12
	2	9	2.89E-07	6.28E-07	9.79E-07	2.42E-07	3.65E-06	1.00E-09	12
	3	8	3.09E-07	1.10E-06	8.49E-07	2.60E-07	6.59E-07	1.00E-08	12
Nb	1	8	3.96E-07	6.11E-07	1.06E-06	2.59E-07	1.21E-07	1.00E-09	12
	2	10	2.93E-07	8.23E-07	8.73E-07	2.62E-07	1.45E-05	1.00E-09	13
	3	9	3.20E-07	1.71E-06	6.22E-07	2.40E-07	3.82E-07	1.00E-09	12
Nt	1	12	1.17E-07	5.84E-07	4.89E-07	1.16E-07	8.91E-08	1.00E-10	15
	2	9	4.95E-07	5.17E-07	8.06E-07	2.46E-07	3.08E-06	1.00E-11	11
	3	11	3.62E-07	9.06E-07	8.49E-07	2.45E-07	2.21E-06	1.00E-09	14
Kr	1	10	3.18E-07	8.04E-07	9.64E-07	2.34E-07	3.07E-07	1.00E-11	12
	2	9	3.10E-07	6.65E-07	5.58E-07	2.79E-07	2.11E-05	1.00E-09	13
	3	9	4.03E-07	7.05E-07	1.35E-06	2.38E-07	5.76E-06	1.00E-11	12
Fr	1	11	4.11E-07	5.79E-07	6.92E-07	2.76E-07	5.64E-06	1.00E-09	12
	2	11	3.73E-07	7.41E-07	5.44E-07	2.68E-07	7.26E-06	1.00E-09	12
	3	10	4.54E-07	4.01E-07	8.08E-07	2.48E-07	6.91E-07	1.00E-09	11
Rd	1	13	2.82E-07	1.28E-06	5.66E-07	2.41E-07	1.10E-06	1.00E-09	12
	2	9	4.50E-07	6.38E-07	1.17E-06	2.54E-07	8.92E-07	1.00E-09	11
	3	10	5.89E-07	5.05E-07	7.28E-06	2.43E-07	9.97E-06	1.00E-11	11

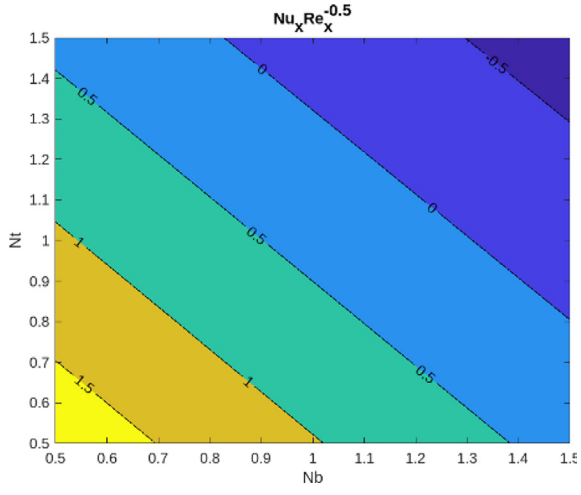

Fig. 10a $Nu_x Re_x^{-0.5}$ VS Nt VS Nb.

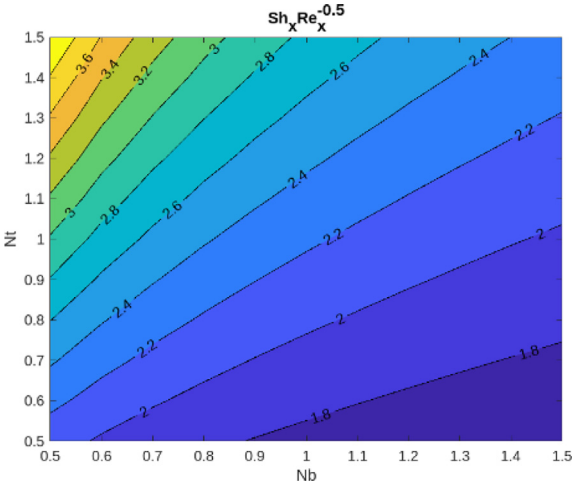

Fig. 10c $Sh_x Re_x^{-0.5}$ VS Nt VS Nb.

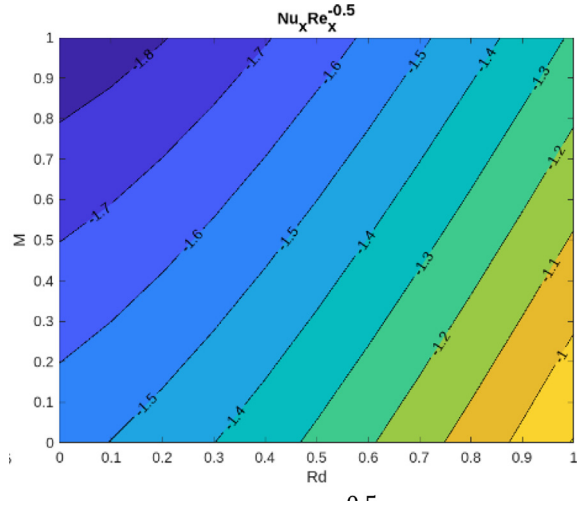

Fig. 10b $Nu_x Re_x^{-0.5}$ VS M VS Rd.

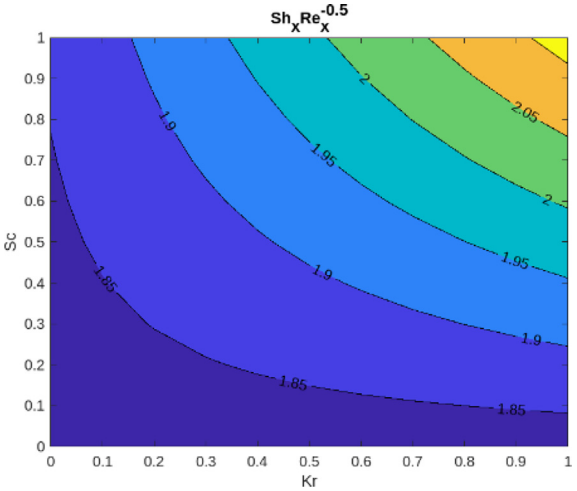

Fig. 10d $Sh_x Re_x^{-0.5}$ VS Sc VS Kr.

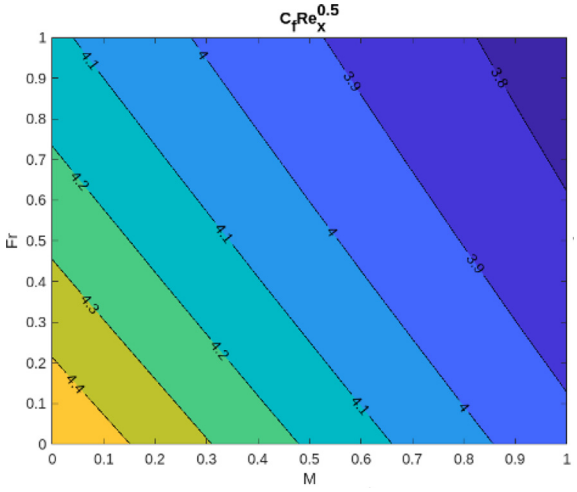

Fig. 10e $Nu_x Re_x^{-0.5}$ VS Fr VS M.

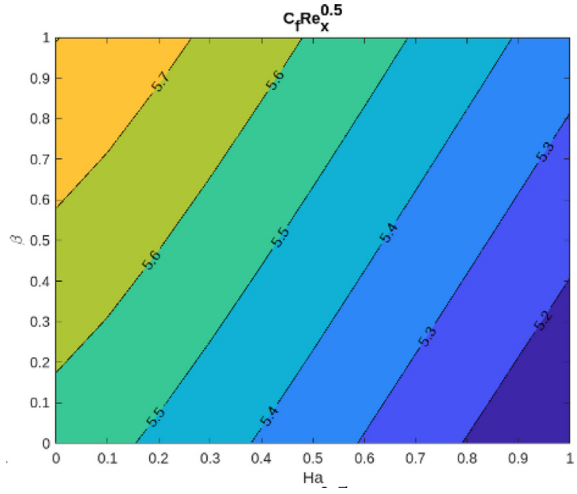

Fig. 10f $Sh_x Re_x^{-0.5}$ VS β VS Ha.

depicts the effect of Nb and Nt on the mass transfer rate. The mass transfer rate increases by increasing values of Nt while, reverse trend is observed for Nb. Fig. 10d shows that mass transfer rate is rising with increasing Kr and Sc. Fig. 10e depicts that the skin friction coefficient increasing by reducing the values of M and Fr. Fig. 10f reveals that the skin friction coefficient increases by increasing the values of β, while reverse effect is observed for Ha.

7. Conclusion

The hybrid nanofluid Ag-Al_2O_3/H_2O flow through a rotating disk is investigated under the combined effect of joule heating, external magnetic field, and viscous dissolution in the presence of Riga surface, thermal radiation, and chemical reaction. The effect of different physical parameters like porosity parameter, Darcy-Forchheimer parameter, Hartmann number, radiation parameter, Brinkman number, Prandtl number, Eckert number, width parameter, Brownian motion parameter, thermophoresis parameter, Schmidt number, and chemical reaction parameter are analysed on velocity, temperature, and concentration profiles. The major outcomes of the present study are as follows:

- The velocity profile decreases by increasing values of the Darcy-Forchheimer parameter and magnetic parameters, while reverse effect is observed for the modified Hartmann number.
- The radial velocity decreases by increasing the concentration of nanoparticles, whereas, the azimuthal velocity initially increases and then reverse trend is observed.
- The temperature profile increases due to increasing values of the Brownian motion and thermophoresis parameters and decreases by increasing the thermal radiation parameter.
- The concentration profile decreases as the values of the thermophoresis parameter increases, whereas opposite behavior is noticed for the values of Brownian motion and chemical reaction parameters.
- The Nusselt number increases by increasing Rd and decreasing M, Nt, and Nb. The Sherwood number increases by decreasing Nb and increasing Nt, Kr, and Sc.

The ANN structure functions are like human brain neurons, which are able to learn from a given input–output set and then apply this learning to predict the output for a new sample input set with high speed and accuracy. There are numerous applications for artificial neural networks, including image recognition, machine translation, and medical diagnosis. A significant advantage of ANN is that it can learn from sample data sets. The results obtained from the study can be used to analyse the heat and mass transfer phenomenon in power plants, to prepare hybrid nanofluids in factories and industries, to make coolants for air conditioners and refrigerators, to prepare batteries for electric vehicles. The base fluid can be changed with blood to study for preparing drugs and medicines. ANN can be used to predict the fluid properties in industries. Engineers and scientists will be able to create more effective, efficient, and cutting-edge fluid systems using ANN, which has the potential to transform fluid mechanics research and development.

Declaration of Competing Interest

The authors declare that they have no known competing financial interests or personal relationships that could have appeared to influence the work reported in this paper.

Acknowledgement

Author U.F.-G. appreciates the support of the Government of the Basque Country, Grant N. ELKARTEK 22/85 and ELKARTEK 21/10.

References

[1] I. Khan, New idea of Atangana and Baleanu fractional derivatives to human blood flow in nanofluids. *Chaos: An Interdisciplinary*, J. Nonlinear Sci. 29 (1) (2019) 013121.
[2] I. Khan, Prabhakar fractional derivative model of sodium alginate (C6H9NaO7) for accelerated plate motions, Front. Energy Res. 10 (2022).
[3] I. Khan, Hemodynamics of blood flow over an inclined cylinder, Waves Random Complex Media (2022) 1–12.

[4] M. Izady, S. Dinarvand, I. Pop, A.J. Chamkha, Flow of aqueous Fe2O3–CuO hybrid nanofluid over a permeable stretching/shrinking wedge: A development on Falkner-Skan problem, Chin. J. Phys. 74 (2021) 406–420.
[5] S. Dinarvand, H. Berrehal, I. Pop, A.J. Chamkha, Blood-based hybrid nanofluid flow through converging/diverging channel with multiple slips effect: a development of Jeffery-Hamel problem, Int. J. Numer. Meth. Heat Fluid Flow 33 (3) (2023) 1144–1160.
[6] I. Khan, Significance of Ramped Temperature in the Dynamics of Unsteady Viscoelastic Fluid Subjected to Lorentz Force. Frontiers, Physics 486 (2022).
[7] S. Dinarvand, S.M. Mousavi, M. Yousefi, M. Nademi Rostami, MHD flow of MgO-Ag/water hybrid nanofluid past a moving slim needle considering dual solutions: An applicable model for hot-wire anemometer analysis, Int. J. Numer. Meth. Heat Fluid Flow 32 (2) (2022) 488–510.
[8] U. Khan, F. Mebarek-Oudina, A. Zaib, A. Ishak, S. Abu Bakar, E.S.M. Sherif, D. Baleanu, An exact solution of a Casson fluid flow induced by dust particles with hybrid nanofluid over a stretching sheet subject to Lorentz forces, Waves Random Complex Media (2022) 1–14.
[9] D. Mohanty, G. Mahanta, S. Shaw, M. Das, Thermosolutal Marangoni stagnation point GO–MoS2/water hybrid nanofluid over a stretching sheet with the inclined magnetic field, Int. J. Mod Phys B 2450024 (2023).
[10] I. Khan, Ramped heating in CNTS fractional nanofluids, Case Studies in Thermal Engineering 45 (2023) 102836.
[11] I. Khan, A. Raza, M.A. Shakir, A.S. Al-Johani, A.A. Pasha, K. Irshad, Natural convection simulation of Prabhakar-like fractional Maxwell fluid flowing on inclined plane with generalized thermal flux, Case Studies in Thermal Engineering 35 (2022) 102042.
[12] H. Berrehal, S. Dinarvand, I. Khan, Mass-based hybrid nanofluid model for entropy generation analysis of flow upon a convectively-warmed moving wedge, Chin. J. Phys. 77 (2022) 2603–2616.
[13] F. Mebarek-Oudina, I. Chabani, Review on nano-fluids applications and heat transfer enhancement techniques in different enclosures, Journal of Nanofluids 11 (2) (2022) 155–168.
[14] S. Dinarvand, M.N. Rostami, Three-dimensional squeezed flow of aqueous magnetite–graphene oxide hybrid nanofluid: a novel hybridity model with analysis of shape factor effects, Proceedings of the Institution of Mechanical Engineers, Part E: Journal of Process Mechanical Engineering 234v(2) (2020) 193–205.
[15] S.S. Samantaray, S. Shaw, A. Misra, M.K. Nayak, J. Prakash, Darcy-Forchheimer up/downflow of entropy optimized radiative nanofluids with second-order slip, nonuniform source/sink, and shape effects, Heat Transfer 51 (2) (2022) 2318–2342.
[16] S.S. Ghadikolaei, M. Yassari, H. Sadeghi, K. Hosseinzadeh, D. D. Ganji, Investigation on thermophysical properties of Tio2–Cu/H2O hybrid nanofluid transport dependent on shape factor in MHD stagnation point flow, Powder Technol. 322 (2017) 428–438.
[17] S.S. Ghadikolaei, K. Hosseinzadeh, D.D. Ganji, Investigation on ethylene glycol-water mixture fluid suspend by hybrid nanoparticles (TiO2-CuO) over rotating cone with considering nanoparticles shape factor, J. Mol. Liq. 272 (2018) 226–236.
[18] S.S. Ghadikolaei, K. Hosseinzadeh, D.D. Ganji, Investigation on three-dimensional squeezing flow of mixture base fluid (ethylene glycol-water) suspended by hybrid nanoparticle (Fe3O4-Ag) dependent on shape factor, J. Mol. Liq. 262 (2018) 376–388.
[19] M. Mansourian, S. Dinarvand, I. Pop, Aqua Cobalt Ferrite/Mn–Zn Ferrite Hybrid Nanofluid Flow Over a Nonlinearly Stretching Permeable Sheet in a Porous Medium, Journal of Nanofluids 11 (3) (2022) 383–391.
[20] H. Ilyas, I. Ahmad, M.A.Z. Raja, M.B. Tahir, M. Shoaib, Neuro-intelligent mappings of hybrid hydro-nanofluid Al2O3–Cu–H2O model in porous medium over rotating disk with viscous dissolution and Joule heating, Int. J. Hydrogen Energy 46 (55) (2021) 28298–28326.
[21] J. Raza, F. Mebarek-Oudina, L. Ali Lund, The flow of magnetised convective Casson liquid via a porous channel with shrinking and stationary walls, Pramana 96 (4) (2022) 229.
[22] S.S. Ghadikolaei, K. Hosseinzadeh, M. Yassari, H. Sadeghi, D. D. Ganji, Analytical and numerical solution of non-Newtonian second-grade fluid flow on a stretching sheet, Thermal Science and Engineering Progress 5 (2018) 309–316.
[23] S.S. Ghadikolaei, K. Hosseinzadeh, M. Hatami, D.D. Ganji, MHD boundary layer analysis for micropolar dusty fluid containing Hybrid nanoparticles (Cu Al2O3) over a porous medium, J. Mol. Liq. 268 (2018) 813–823.
[24] S.S. Ghadikolaei, K. Hosseinzadeh, D.D. Ganji, M. Hatami, Fe3O4–(CH2OH) 2 nanofluid analysis in a porous medium under MHD radiative boundary layer and dusty fluid, J. Mol. Liq. 258 (2018) 172–185.
[25] S.S. Ghadikolaei, K. Hosseinzadeh, M. Yassari, H. Sadeghi, D. D. Ganji, Boundary layer analysis of micropolar dusty fluid with TiO2 nanoparticles in a porous medium under the effect of magnetic field and thermal radiation over a stretching sheet, J. Mol. Liq. 244 (2017) 374–389.
[26] A. Shafiq, F. Mebarek-Oudina, T.N. Sindhu, G. Rasool, Sensitivity analysis for Walters-B nanoliquid flow over a radiative Riga surface by RSM, Sci. Iran. 29 (3) (2022) 1236–1249.
[27] N. Abbas, W. Shatanawi, K.U. Rehman, T.A. Shatnawi, Velocity and thermal slips impact on boundary layer flow of micropolar nanofluid over a vertical nonlinear stretched Riga sheet, Proceedings of the Institution of Mechanical Engineers, Part N: Journal of Nanomaterials, Nanoengineering and Nanosystems 23977914231156685 (2023).
[28] W. Shatanawi, N. Abbas, T.A. Shatnawi, F. Hasan, Heat and mass transfer of generalized fourier and Fick's law for second-grade fluid flow at slendering vertical Riga sheet, Heliyon 9 (3) (2023).
[29] N. Abbas, S. Nadeem, A. Sial, W. Shatanawi, Numerical analysis of generalized Fourier's and Fick's laws for micropolar Carreaufluid over a vertical stretching Riga sheet, ZAMM-Journal of Applied Mathematics and Mechanics/Zeitschrift für Angewandte Mathematik und Mechanik 103 (2) (2023) e202100311.
[30] N. Abbas, W. Shatanawi, T.A. Shatnawi, Theoretical analysis of modified non-Newtonian micropolar nanofluid flow over vertical Riga sheet, Int. J. Mod Phys B 37 (02) (2023) 2350016.
[31] S. Nadeem, M. Tumreen, B. Ishtiaq, N. Abbas, W. Shatanawi, Second-grade nanofluid flow above a vertical slandering Riga surface with double diffusion model, Int. J. Mod Phys B 36 (32) (2022) 2250237.
[32] G. Dharmaiah, F. Mebarek-Oudina, M.S. Kumar, K.C. Kala, Nuclear reactor application on Jeffrey fluid flow with Falkner-skan factor, Brownian and thermophoresis, non linear thermal radiation impacts past a wedge, J. Indian Chem. Soc. 100 (2) (2023) 100907.
[33] K. Swain, B. Mahanthesh, F. Mebarek-Oudina, Heat transport and stagnation-point flow of magnetized nanoliquid with variable thermal conductivity, Brownian moment, and thermophoresis aspects, Heat Transfer 50 (1) (2021) 754–767.
[34] I. Chabani, F. Mebarek-Oudina, H. Vaidya, A.I. Ismail, Numerical analysis of magnetic hybrid Nano-fluid natural

convective flow in an adjusted porous trapezoidal enclosure, J. Magn. Magn. Mater. 564 (2022) 170142.
[35] F. Mebarek-Oudina, Convective heat transfer of Titania nanofluids of different base fluids in cylindrical annulus with discrete heat source. Heat Transfer—Asian, Research 48 (1) (2019) 135–147.
[36] S.K. Sahu, S. Shaw, D.N. Thatoi, M. Azam, M.K. Nayak, Darcy-Forchheimer flow behavior and thermal inferences with SWCNT/MWCNT suspensions due to shrinking rotating disk, Waves Random Complex Media (2022) 1–29.
[37] M.K. Nayak, S. Shaw, H. Waqas, T. Muhammad, Numerical computation for entropy generation in Darcy-Forchheimer transport of hybrid nanofluids with Cattaneo-Christov double-diffusion, Int. J. Numer. Meth. Heat Fluid Flow 32 (6) (2022) 1861–1882.
[38] S.S. Ghadikolaei, M. Gholinia, M.E. Hoseini, D.D. Ganji, Natural convection MHD flow due to MoS2–Ag nanoparticles suspended in C2H6O2H2O hybrid base fluid with thermal radiation, J. Taiwan Inst. Chem. Eng. 97 (2019) 12–23.
[39] S.S. Ghadikolaei, K. Hosseinzadeh, D.D. Ganji, Investigation on Magneto Eyring-Powell nanofluid flow over inclined stretching cylinder with nolinear thermal radiation and Joule heating effect. World, J. Eng. (2019).
[40] S.S. Ghadikolaei, K. Hosseinzadeh, D.D. Ganji, Numerical study on magnetohydrodynic CNTs-water nanofluids as a micropolar dusty fluid influenced by non-linear thermal radiation and joule heating effect, Powder Technol. 340 (2018) 389–399.
[41] S.S. Ghadikolaei, K. Hosseinzadeh, M. Hatami, D.D. Ganji, M. Armin, Investigation for squeezing flow of ethylene glycol (C2H6O2) carbon nanotubes (CNTs) in rotating stretching channel with nonlinear thermal radiation, J. Mol. Liq. 263 (2018) 10–21.
[42] S.S. Ghadikolaei, K. Hosseinzadeh, D.D. Ganji, B. Jafari, Nonlinear thermal radiation effect on magneto Casson nanofluid flow with Joule heating effect over an inclined porous stretching sheet, Case studies in thermal engineering 12 (2018) 176–187.
[43] S.S. Ghadikolaei, K. Hosseinzadeh, D.D. Ganji, Analysis of unsteady MHD Eyring-Powell squeezing flow in stretching channel with considering thermal radiation and Joule heating effect using AGM, Case studies in thermal engineering 10 (2017) 579–594.
[44] S.S. Samantaray, A. Misra, S. Shaw, J. Prakash, V.S. Pandey, M.K. Nayak, Investigating to chemically reactive and radiative Darcy/non-Darcy stagnation point flow of ternary composite nanofluids with moderate Prandtl numbers, Int. J. Model. Simul. (2023) 1–17.
[45] S.K. Sahu, S. Rout, S. Shaw, N. Dash, D.N. Thatoi, M.K. Nayak, Hydrothermal stagnation point flow of Carreau nanofluid over a moving thin needle with non-linear Navier's slip and cubic autocatalytic chemical reactions in Darcy-Forchheimer medium, J. Indian Chem. Soc. 99 (11) (2022) 100741.
[46] D. Mohanty, G. Mahanta, S. Shaw, Analysis of irreversibility for 3-D MHD convective Darcy-Forchheimer Casson hybrid nanofluid flow due to a rotating disk with Cattaneo-Christov heat flux, Joule heating, and nonlinear thermal radiation, in: B. Part (Ed.), Numerical Heat Transfer, Fundamentals, 2023, pp. 1–28.
[47] S.K. Sahu, S. Shaw, D.N. Thatoi, M.K. Nayak, A thermal management of Darcy-Forchheimer SWCNT–MWCNT Cross hybrid nanofluid flow due to vertical stretched cylinder with and without inertia effects, Waves Random Complex Media (2022) 1–27.
[48] N. Abbas, K.U. Rehman, W. Shatanawi, M.Y. Malik, Numerical study of heat transfer in hybrid nanofluid flow over permeable nonlinear stretching curved surface with thermal slip, Int. Commun. Heat Mass Transfer 135 (2022) 106107.
[49] A. Shafiq, A.B. Çolak, T.N. Sindhu, Significance of EMHD graphene oxide (GO) water ethylene glycol nanofluid flow in a Darcy-Forchheimer medium by machine learning algorithm, The European Physical Journal Plus 138 (3) (2023) 213.
[50] A. Shafiq, A.B. Çolak, T.N. Sindhu, Modeling of Soret and Dufour's convective heat transfer in nanofluid flow through a moving needle with artificial neural network, Arab. J. Sci. Eng. (2022) 1–14.
[51] A. Shafiq, A.B. Çolak, T. Naz Sindhu, Designing artificial neural network of nanoparticle diameter and solid–fluid interfacial layer on single-walled carbon nanotubes/ethylene glycol nanofluid flow on thin slendering needles, Int. J. Numer. Meth. Fluids 93 (12) (2021) 3384–3404.
[52] A. Shafiq, A.B. Çolak, T.N. Sindhu, Q.M. Al-Mdallal, T. Abdeljawad, Estimation of unsteady hydromagnetic Williamson fluid flow in a radiative surface through numerical and artificial neural network modeling, Sci. Rep. 11 (1) (2021) 14509.
[53] Çolak, A. B., Sindhu, T. N., Lone, S. A., Akhtar, M. T., & Shafiq, A. A comparative analysis of maximum likelihood estimation and artificial neural network modeling to assess electrical component reliability. Quality and Reliability Engineering International.
[54] A. Shafiq, A.B. Çolak, C. Swarup, T.N. Sindhu, S.A. Lone, Reliability analysis based on mixture of lindley distributions with artificial neural network, Advanced Theory and Simulations 5 (8) (2022) 2200100.
[55] A. Shafiq, A.B. Çolak, T.N. Sindhu, Analyzing activation energy and binary chemical reaction effects with artificial intelligence approach in axisymmetric flow of third grade nanofluid subject to Soret and Dufour effects, Heat Transfer Research 54 (3) (2023).
[56] A. Shafiq, A.B. Çolak, T.N. Sindhu, S.A. Lone, A. Alsubie, F. Jarad, Comparative study of artificial neural network versus parametric method in COVID-19 data analysis, Results Phys. 38 (2022) 105613.
[57] T. Hayat, F. Haider, T. Muhammad, A. Alsaedi, On Darcy-Forchheimer flow of carbon nanotubes due to a rotating disk, Int. J. Heat Mass Transf. 112 (2017) 248–254, https://doi.org/10.1016/j.ijheatmasstransfer.2017.04.123.
[58] G. Seth, R. Kumar, A. Bhattacharyya, Entropy generation of dissipative flow of carbon nanotubes in rotating frame with Darcy-Forchheimer porous medium: A numerical study, J. Mol. Liq. 268 (2018), https://doi.org/10.1016/j.molliq.2018.07.071.
[59] M. Mustafa, MHD nanofluid flow over a rotating disk with partial slip effects: Buongiorno model, Int. J. Heat Mass Transf. 108 (2017) 1910–1916, https://doi.org/10.1016/j.ijheatmasstransfer.2017.01.064.
[60] M. Ramzan, M. Javed, S. Rehman, D. Khan, A. Saeed, P. Kumam, Computational assessment of microrotation and buoyancy effects on the stagnation point flow of carreau–yasuda hybrid nanofluid with chemical reaction past a convectively heated riga plate, ACS Omega 7 (2022), https://doi.org/10.1021/acsomega.2c03570.
[61] S.S. Ghadikolaei, M. Gholinia, Terrific effect of H2 on 3D free convection MHD flow of C2H6O2H2O hybrid base fluid to dissolve Cu nanoparticles in a porous space considering the thermal radiation and nanoparticle shapes effects, Int. J. Hydrogen Energy 44 (31) (2019) 17072–17083.
[62] S.S. Ghadikolaei, M. Gholinia, 3D mixed convection MHD flow of GO-MoS2 hybrid nanoparticles in H2O–(CH2OH) 2 hybrid base fluid under the effect of H2 bond, Int. Commun. Heat Mass Transfer 110 (2020) 104371.
[63] R. Gandhi, B.K. Sharma, N. Mishra, Q. Al-Mdallal, Computer simulations of EMHD Casson nanofluid flow of blood through an irregular stenotic permeable artery, Application of Koo-

Kleinstreuer-Li Correlations. 13 (2023) 652, https://doi.org/10.3390/nano13040652.

[64] B.K. Sharma, A. Kumar, R. Gandhi, M.M. Bhatti, N. Mishra, Entropy Generation and Thermal Radiation Analysis of EMHD Jeffrey Nanofluid Flow: Applications in Solar Energy, Nanomaterials 13 (2023) 544, https://doi.org/10.3390/nano13030544.

[65] B.K. Sharma, R. Gandhi, N. Mishra, Q. Al-Mdallal, Entropy generation minimization of higher-order endothermic/exothermic chemical reaction with activation energy on MHD mixed convective flow over a stretching surface, Sci. Rep. 12 (2022), https://doi.org/10.1038/s41598-022-22521-5.

[66] R. Gandhi, B.K. Sharma, C. Kumawat, O.A. Bég, Modeling and analysis of magnetic hybrid nanoparticle (Au-Al2O3/blood) based drug delivery through a bell-shaped occluded artery with Joule heating, viscous dissipation and variable viscosity effects, Proceedings of the Institution of Mechanical Engineers, Part E: Journal of Process Mechanical Engineering. (2022).

[67] Sharma, Bhupendra; Poonam; Chamkha, Ali. (2022). Effects of heat transfer, body acceleration and hybrid nanoparticles (Au–Al 2 O 3) on MHD blood flow through a curved artery with stenosis and aneurysm using hematocrit-dependent viscosity. Waves in Random and Complex Media. 1-31. 10.1080/17455030.2022.2125597.

[68] B.K. Sharma, R. Gandhi, Combined effects of Joule heating and non-uniform heat source/sink on unsteady MHD mixed convective flow over a vertical stretching surface embedded in a Darcy-Forchheimer porous medium, Propul. Power Res. 11 (2022), https://doi.org/10.1016/j.jppr.2022.06.001.

[69] B.K. Sharma, C. Kumawat, O. Makinde, Hemodynamical analysis of MHD two phase blood flow through a curved permeable artery having variable viscosity with heat and mass transfer, Biomech. Model. Mechanobiol. 21 (2022), https://doi.org/10.1007/s10237-022-01561-w.

[70] Poonam; Sharma, B K; Kumawat, Chandan; Vafai, Kambiz. (2022). Computational biomedical simulations of hybrid nanoparticles (Au - Al 2 O 3 / blood-mediated) transport in a stenosed and aneurysmal curved artery with heat and mass transfer: Hematocrit dependent viscosity approach. Chemical Physics Letters. 800. 139666. 10.1016/j.cplett.2022.139666.